Synthesis and Functionality of Freestanding Perovskite Oxide Sheets Using Amorphous Oxide Protection Layer

アモルファス酸化物保護層を用いた自立型ペロブスカイト酸化物シートの合成と機能性

LIZHIKUN GONG

Graduate School of Information Science and Technology

Hokkaido University

March 2024

Table of Contents

List of Figures

List of Acronyms

LSSO	La-doped $SrSnO_3$
DUV	deep-ultraviolet
LBSO	La-doped $BaSnO_3$
BTO	$BaTiO_3$
BST	$Ba_{1-x}Sr_xTiO_3$
STO	$SrTiO_3$
SAO	$Sr_3Al_2O_6$
a-	amorphous
ITO	Full width at half maximum
PLD	pulsed laser deposition
ITO	In-doped tin oxide
XRD	X-ray diffraction
FWHM	Full width at half maximum
AFM	atomic force microscope
SEM	scanning electron microscope
IGZO	indium gallium zinc oxide
TCOs	transparent conducting oxides
RSM	reciprocal space mapping
PET	polyethylene terephthalate
RT	room temperature
LCR	inductance, capacitance, resistance (meter)
Poly-	Polycrystal
XRR	X-ray reflectivity

Lis of symbols

E_g	bandgap
σ	electrical conductivity
ε_r	dielectric permittivity
t_{cap}	protection layer thickness
t_{film}	perovskite oxide film thickness
T_S	substrate temperature
P_{O2}	oxygen pressure
a_{bulk}	*a*-axis length of bulk single-crystal
c_{bulk}	*c*-axis length of bulk single-crystal
a	*a*-axis length
c	*c*-axis length
T	optical transmission
R	optical reflection
q_z	scattering vector
P	polarization
C	capacitance
$\tan\delta$	dielectric loss
d_{33}	piezoelectric coefficient
x	stoichiometry
P_r	remnant polarization
λ	wavelength
h	Plank's constant
α	absorption coefficient
v	speed of light

Chapter 1. General Introduction

1.1. Functional Perovskite Oxide Films

Perovskite oxides with the general formula ABO_3—where A is an alkaline earth or rare earth metal and B is a transition metal. The basic perovskite structure can be defined as a cubic unit cell where the B-site cation is located at the center of the cube, the A-site cation is at the corners, and the O anions are the middle of the plane faces (*1, 2*). This leads to the B site ion are octahedrally coordinated to O atoms, and the BO_6 octahedra share corner across to the 3 dimensions of the lattice. Through the selection of the A- and B-site cations, various distinct properties can be realized, such as a giant dielectric permittivity (*3-5*), ferroelectricity (*6, 7*), piezoelectricity (*8, 9*), pyroelectricity (*10, 11*), ferromagnetism (*12, 13*), multiferroicity (*14, 15*), high catalytic activity (*16, 17*), superconductivity (*18, 19*), high electron mobility (*20, 21*), and high transparent electric conductivity (*22, 23*). Because of the excellent properites, perovskite oxides have hold extensive applications in the field of electronic devices, including sensors (*24*), capacitors (*25*), piezoelectric devices (*26*), memory devices (*27*), high-temperature superconductor and more (*28*). The functionalities of perovskite oxides are decided from the interaction between the charge, orbital, spin, and lattice properties.

These functional perovskite oxides have also been extensively utilized in a form of thin films, which is essential for the application of miniaturized electronics devices. However,

these fruitful properties of perovskite oxide thin films are strongly related to their growth orientation and crystallinity, thus, highly-oriented films are necessary. Single-crystal substrates are usually used to epitaxial grow those highly-oriented thin films. And the selection of the single-crystal substrates is also important because unmatched lattice symmetry between the substrate and film can cause deterioration in the properties. Therefore, a well-regulated epitaxial growth over the material heterointerface between perovskite oxide thin films and substrates is essential. Currently, duo to the strict growing conditions mentioned above, fabrication of perovskite oxide thin films on large-scale substrates such as Si wafer, glass, polymer, metal, and flexible substrate is still challenging. Thus, the solutions to obtain high single-crystallized perovskite oxide thin films on these substrates are urgently demanded.

1.2. Functionality of Freestanding Perovskite Oxide Sheet

Recently, the peeled-off and transfer method has emerged as a promising technique for synthesizing freestanding perovskite oxide sheets (*29*). In this method, the objective perovskite oxide film is first fabricated in the single-crystal form on a sacrificial layer buffered single-crystal substrates, after which the film is peeled off from the substrate by etching the sacrificial layer (*29*), and transferred onto designed substrates. Through this method, ultra-thin single crystal oxide can be prepared, resulting in unveiling many hidden physical properties and outstanding performance. For example, D. Ji et al. reported a synthesis of monolayer of freestanding crystalline oxide perovskites, and found the unexpected giant tetragonality and polarization in 3 units cell thick of $BiFeO_3$ sheet with large *c*/*a* value of 1.22 (*30*). In addition, G. Dong et al. reported super-elastic property in ultra-thin freestanding $BaTiO_3$ (BTO) sheet which can be bent over 180° and recover, which is in contrast to previously common sense of oxides which should be rigid and brittle under deformation (*31*). Extreme tensile strain exceeding 8% uniaxially and 5% biaxially was also achieved in a freestanding $La_{0.7}Ca_{0.3}MnO_3$ sheet, resulting in a large reduction of the ferromagnetic interaction (*32*). Similarly, the freestanding $SrTiO_3$ (STO) sheet exhibited room-temperature ferroelectricity by applying 2% uniaxial tensile strain (*33*). R. Guo et al. revealed the flexoelectricity in the freestanding $BiFeO_3$ sheet through bending on flexible substrate (*34*). A giant piezoelectricity was also confirmed in the freestanding BTO freestanding sheet, and more interestingly, the sheet can roll under

irradiation of electron beam (*35*). In the aspect of outstanding performance, a high-k STO freestanding sheet was successfully integrated as insulation layer for two-dimensional transistors (*36*). The ultrathin piezoelectric resonators based on freestanding BTO sheet are also reported to show outstanding high resonance frequency over 233 GHz (*37*). In addition, beside above studies, many functional freestanding perovskite oxide sheets have been reported thus far, such as ferromagnetic perovskite manganates (*38*), or $SrRuO_3$ (*39*), $Pb(Zr, Ti)O_3$ (*40*), $YBa_2Cu_3O_{7-x}$ (*41*), and transparent conductive $La:BaSnO_3$ (LBSO) (*42, 43*), $La:SrSnO_3$ (LSSO) have been obtained (*44*). These findings demonstrate the lifted-off and transfer method high penitential to achieve next generation high performance devices, by overcoming the difficulty of highly crystalline perovskite oxide films to integrate on particularly Si substrate without applying high synthesis temperature and limitation of lattice mismatch between the film and substrate.

1.3. Synthesis of Freestanding Perovskite Oxide Sheets

1.3.1 Wet Etching of Sacrificial Layers

To obtain the freestanding perovskite oxide sheet, there are three main transfer methods: wet etching of sacrificial layer, mechanical exfoliation, and self-formed freestanding films through spalling, respectively. Among them, wet etching of sacrificial layer is promising to obtain large-area and high-quality single-crystal freestanding perovskite oxide sheets. In this method, the target perovskite film is firstly grown on top of a sacrificial layer buffered substrate which is able to be dissolved by etching.

Recently, a new emerging sacrificial layer $Sr_3Al_2O_6$ (SAO) has attracted attention owing to its water-solubility and crystal structure. SAO has a cubic structure (space group *Pa*3) with lattice constant equal with (a/4 = 0.3961 nm) (*45-47*), which is compatibility well with other perovskite oxides such as $SrTiO_3$ with a cubic structure with a = 0.3905 nm. Therefore, SAO is widely used as a water-soluble sacrificial layer to fabricate freestanding perovskite oxide sheet; indeed, many researches shown above have used the SAO sacrificial layer. This method allows transfer of ultrathin single crystal sheets even down to few unit cells, or thicker film up to several hundred nanometers (*30, 44*). In addition, one other advantage of SAO is that by controlling the ratio between Ca, Sr, and Ba, respectively can modify the lattice parameter of sacrificial layer to find perfectly matched composite of the sacrificial layer, which can largely improve the quality of the transferred perovskite sheets (*32, 33, 43*). However, the dissolving capacity in pure water

have a relationship with doping ratio that decrease with increasing Ca ratio, and increase with increasing Ba ratio. For example, 20 nm SAO sacrificial layer can be completely dissolved in pure water around 2 h (*44*), while a $Ba_3Al_2O_6$ sacrificial layer only takes few minutes (*43*). To the contrary, $Ca_3Al_2O_6$ sacrificial layer spends several days to be completely dissolved (*29*). In the fabrication possess, the pulsed layer deposition (PLD) and molecular beam epitaxy (MBE) are usually used to prepare a high crystalline perovskite oxide film on SAO buffered single-crystal substrate (*46, 48*).

Perovskite oxides have also been used as wet etching sacrificial layer such as $La_xSr_{1-x}MnO_3$ (LSMO) (*49-51*), SRO (*52*), $SrVO_3$ (*53*), and $SrCoO_{2.5}$ (*40, 54*). Different with SAO, these materials have the same perovskite structure with target perovskite film, which improves crystal quality of the films due to the lattice matching. However, etching of these material needs complex solvent. For example, LSMO cannot dissolve in pure water but an aqueous solution of KI + HCl + H_2O in following chemical equation (*55*):

$$MnO_2 + 4H_3O^+ + 2Cl^- \rightarrow Mn^{2+} + 6H_2O + Cl_2$$

And there is residual problem of MnO_2, which influence the transferred sheet further integration with devices. Beside perovskite oxides sacrificial layer, metal oxide such as BaO (*56*), MgO (*57*), ZnO (*58*), and VO_2 (*59*) have also been studied as wet etching sacrificial layer, also not comparable with SAO in the term of dissolving time. Thus, many researchers focus on using SAO as sacrificial layer to fabricate freestanding perovskite oxide sheets.

1.3.2 Transfer Methods of Freestanding Perovskite Oxide Sheets

Transfer methods is also important to obtain high quality freestanding perovskite oxide sheets. Currently, main transfer method to obtain freestanding sheet is combined the water-soluble sacrificial layer to release the sheet and polymer supporter layer to transfer sheet on other substrate, which follow suit from well-known wet transfer process of 2D vdW materials (*60, 61*). This kind of transfer methods can be divided in four main steps: stick the polymer supporter layer on an as-grown film, peered-off the sheet from the substrate, transferring the sheet onto a designed substrate, and removing the supporter layer.

As for the first step, polymer supporter layer such as polymethyl-methacrylate (PMMA), polydimethylsiloxane (PDMS), Polyimide (PI) tape, or adhesive-coated polyethylene terephthalate (PET) are used to cover the as-grown film as shown in **Figure 1-1(a, b)**. The polymer supporter layers can prevent the sheets from dispersing, crinkling, and folding during the etching of the sacrificial layer. After placing the as-grown film into pure water, and completely remove the sacrificial layer, the sheet can be transferred with the polymer supporter layer. If the PMMA or PDMS are used, the sheet can be further stamp and transferred onto designed substrate after post-treatment (**Figure 1-1(a)**). The permanent supporter polymer cannot be removed after peering off (**Figure 1-1(b)**).

PMMA is the most commonly used in this transfer method as a supporter layer, owing to its high harness which can protect sheet during the peeled-off and transfer process and

its easy fabrication condition. However, although the PMMA can be cleared away by acetone after the transfer, PMMA cannot be completely washed away causing polymer residues remain on the surface, resulting in a difficulty in further integrating device on the sheets. Thermal release polymer PDMS is much easier to be removed from the sheet through post annealing up to 70°C, but cracks and winkles often generates inevitably due to its softness. PI tape and adhesive-coated polyethylene terephthalate (PET) are also used as both polymer supporter layer and flexible substrate. However, unlike PMMA and PDMS, they cannot be removed after the transfer (*29*).

Consequently, conventional transfer method using polymer supporter layer cannot fundamentally solve the crack problem during the transfer of freestanding oxide sheet. Thus, developing new transfer method is still highly demanded.

1.3.3 Crack Problem in Sheet and Amorphous Oxide Protection Layers

As I mentioned above, a crucial problem in the peeled-off and transfer method of perovskite oxide sheet is the difficulty of suppressing cracks during the synthesis. To solve of this problem, it is important to fundamentally understand the reason why cracks occur during the dissolving of the SAO sacrificial layer. LSSO (a = 0.4036 nm) and LBSO (a = 0.4116 nm) have much larger lattice constant than SAO (a/4 = 0.3961 nm). When these films epitaxially grown on SAO buffer substrates, larger compressive strain will be applied to the perovskite layers. Therefore, during the dissolution of the sacrificial layer, the substrate-induced strain is released, which applies a retained force to the sheet. This force makes the freestanding sheet into many pieces as shown in **Figure 2-1**. Thus, as pointed out by Chiabrera *et al*., developing a technique for transferring single-crystal oxide sheets with large size, as-grown uniformity, and high quality is a key challenge (*29*). To suppress crack generation, it is useful to change the lattice constant of the SAO sacrificial layer by chemical substitution; for example, a millimeter-sized $BaSnO_3$ sheet was obtained using a $Ba_3Al_2O_6$ sacrificial layer (*43*). However, for practical applications, a simpler and more effective method is required. In addition, in tetragonal ferroelectric materials such as BST and BTO, there exist *a*-axis domains that receive a large strain between *c*-axis domains even if the lattice constant is controlled. Thus, after the restraint from the substrate is removed, a force is applied to the sheet to restore the *a*-axis domains that are largely distorted, resulting in the generation of cracks (*47*).

Basing on this crack mechanism, I come up with an idea that preparation of a hard protection amorphous oxide layer on the perovskite oxide sheet is useful to suppress the crack generation (**Figure 1-1(c)**). One candidate of the protection layer is amorphous Al_2O_3 because Al_2O_3 is very hard material in the world, possessing Mohs hardness of 9 in single-crystal form (Alias: Sapphire). Even in the amorphous state, Al_2O_3 exhibits high Young's modulus (*62*). In addition, there are reports that Al_2O_3-SiO_2 glass shows high crack resistance (*63*).

1.4. Purpose of this thesis

The aim of this doctoral thesis is to investigate the transfer of high-quality, high-performance, and large-area flexible single-crystal epitaxial sheets by using an easily preparable amorphous oxide protective layer, building upon existing lift-off and transfer techniques. In my thesis, I studied LSSO, LBSO, and BST sheets as as typical perovskite oxides and further explored their applications. Through this new transfer method using amorphous oxide protection layer, I successfully transferred the targeted the three materials, all of them exhibiting large crack-free area, and excellent performance.

This doctoral thesis comprises five chapters. Firstly, I would like to provide a brief overview of the core contents in each chapter. The chapter 1 contains the research background and objectives of this study. In chapter 2, I detail the effects of three different amorphous oxide protective layers (a-Al_2O_3, a-ITO, and a-TiO_2, respectively) in transfer of LSSO sheets, and found the effectiveness of a-Al_2O_3 protection layers is most effective for suppressing cracks generation. Freestanding LSSO sheets with a-Al_2O_3 protection layer can stand, also repeatedly bend, demonstrating remarkable elasticity and flexibility. In chapter 3, I successfully transferred large-area (5×5 mm^2) and crack-free LBSO sheets using a-Al_2O_3 protection layers, despite significant lattice mismatch between LBSO (a = 0.4116 nm) and the sacrificial layer SAO (a/4 = 0.3961 nm), proving the high effectiveness of the a-Al_2O_3 protection layer in suppressing cracks from lattice strain. In chapters 4, I successfully transferred large-area (5×5 mm^2) and crack-free BST sheets

using a-Al_2O_3 protection layers, indicating a-Al_2O_3 protection layers are effective to solve cracking problem in ferroelectric oxide sheets. However, the scanning electron microscope (SEM) observations revealed that, in place of cracks, wrinkles were formed between up/down domains along the polarization direction to release lattice distortion. Compared to conventional transfer methods, utilizing a-Al_2O_3 protection layer enables the fabrication of freestanding ferroelectric sheets which exhibit excellent properties comparable to bulk single crystal. Finally, in the chapter 5, overall results of this thesis are summarized. My thesis contributes a new transfer method to obtain large-size, and high-quality freestanding sheets, based on which there may have high chance to further find the significant physical properties hidden in perovskite freestanding sheets.

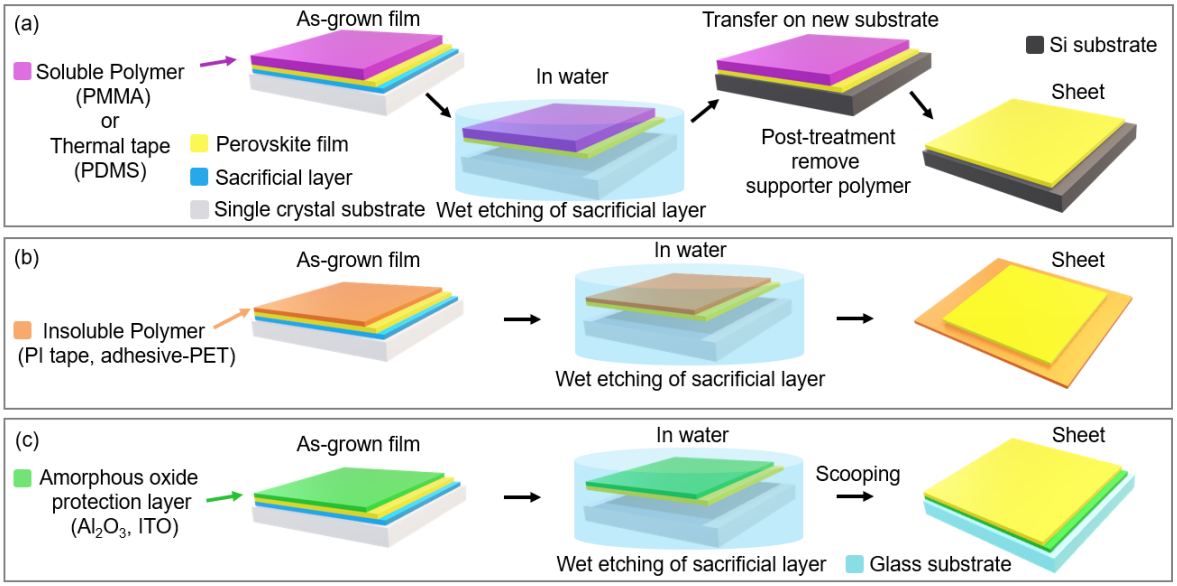

Figure 1-1. Transfer method of freestanding perovskite oxide sheets. Protection layer using (a) soluble polymer or thermal tape, (b) insoluble polymer, and (c) amorphous oxide layer.

Reference

1. H. D. Megaw, Crystal structure of double oxides of the perovskite type. *Proc. Phys. Soc.* **58**, 133 (1946).

2. T. Ishihara, Structure and properties of perovskite oxides. *Perovskite Oxide for Solid Oxide Fuel Cells*, 1–16 (2009).

3. L. Zhao *et al.*, Giant dielectric phenomenon of $Ba_{0.5}Sr_{0.5}TiO_3/CaCu_3Ti_4O_{12}$ multilayers due to interfacial polarization for capacitor applications. *J. Eur. Ceram. Soc.* **39**, 1116–1121 (2019).

4. B. Su, J. Holmes, C. Meggs, T. Button, Dielectric and microwave properties of barium strontium titanate (BST) thick films on alumina substrates. *J. Eur. Ceram. Soc.* **23**, 2699–2703 (2003).

5. T. Hu, J. Juuti, H. Jantunen, T. Vilkman, Dielectric properties of BST/polymer composite. *J. Eur. Ceram. Soc.* **27**, 3997–4001 (2007).

6. K. J. Choi *et al.*, Enhancement of ferroelectricity in strained $BaTiO_3$ thin films. *Science* **306**, 1005–1009 (2004).

7. R. E. Cohen, Origin of ferroelectricity in perovskite oxides. *Nature* **358**, 136–138 (1992).

8. K. Uchino, Glory of piezoelectric perovskites. *Science and Technology of Advanced Materials*, (2015).

9. T. Furukawa, K. Ishida, E. Fukada, Piezoelectric properties in the composite systems of polymers and PZT ceramics. *J. Appl. Phys.* **50**, 4904–4912 (1979).

10. Y. Bai, T. Siponkoski, J. Peräntie, H. Jantunen, J. Juuti, Ferroelectric, pyroelectric, and piezoelectric properties of a photovoltaic perovskite oxide. *Appl. Phys. Lett.* **110**, (2017).

11. N. Ma, Y. Yang, Enhanced self-powered UV photoresponse of ferroelectric $BaTiO_3$ materials by pyroelectric effect. *Nano Energy* **40**, 352–359 (2017).

12. J.-S. Zhou, L. Marshall, Z.-Y. Li, X. Li, J.-M. He, Weak ferromagnetism in perovskite

oxides. *Phys. Rev. B.* **102**, 104420 (2020).

13. N. Ganguli, P. J. Kelly, Tuning ferromagnetism at interfaces between insulating perovskite oxides. *Phys. Rev. Lett.* **113**, 127201 (2014).

14. H. S. Bhatti, S. T. Hussain, F. A. Khan, S. Hussain, Synthesis and induced multiferroicity of perovskite $PbTiO_3$; a review. *Appl. Surf. Sci.* **367**, 291–306 (2016).

15. Y.-D. Liou *et al.*, Deterministic optical control of room temperature multiferroicity in $BiFeO_3$ thin films. *Nat. Mater.* **18**, 580–587 (2019).

16. N. Labhasetwar *et al.*, Perovskite-type catalytic materials for environmental applications. *Science and technology of advanced materials*, (2015).

17. P. Wang *et al.*, Impact of oxygen vacancy occupancy on piezo-catalytic activity of $BaTiO_3$ nanobelt. *Appl. Catal. B: Environ.* **279**, 119340 (2020).

18. K. Ahadi *et al.*, Enhancing superconductivity in $SrTiO_3$ films with strain. *Science advances* **5**, eaaw0120 (2019).

19. A. Baratoff, G. Binnig, Mechanism of superconductivity in $SrTiO_3$. *Physica B+C* **108**, 1335–1336 (1981).

20. W.-J. Lee *et al.*, Transparent perovskite barium stannate with high electron mobility and thermal stability. *Annu. Rev. Mater. Sci.* **47**, 391–423 (2017).

21. A. Prakash, B. Jalan, Wide Bandgap Perovskite Oxides with High Room - Temperature Electron Mobility. *Adv. Mater. Interfaces* **6**, 1900479 (2019).

22. H. J. Kim *et al.*, Physical properties of transparent perovskite oxides (Ba, La)SnO_3 with high electrical mobility at room temperature. *Phys. Rev. B.* **86**, 165205 (2012).

23. M. Wei *et al.*, High electrical conducting deep-ultraviolet-transparent oxide semiconductor La-doped $SrSnO_3$ exceeding ~ 3000 S cm^{-1}. *Appl. Phys. Lett.* **116**, 022103 (2020).

24. J. W. Fergus, Perovskite oxides for semiconductor-based gas sensors. *Sens. Actuators B Chem.* **123**, 1169–1179 (2007).

25. J. Jo, Y. Kim, T. Noh, J.-G. Yoon, T. Song, Coercive fields in ultrathin $BaTiO_3$

capacitors. *Appl. Phys. Lett.* **89**, 232909 (2006).

26. G. L. Smith *et al.*, PZT-based piezoelectric MEMS technology. *J. Am. Ceram. Soc.* **95**, 1777–1792 (2012).

27. Z. Yan, Y. Guo, G. Zhang, J. M. Liu, High-performance programmable memory devices based on co-doped $BaTiO_3$. *Adv. Mater.* **23**, 1351–1355 (2011).

28. C. Rao, Perovskite oxides and high-temperature superconductivity. *Ferroelectrics* **102**, 297–308 (1990).

29. F. M. Chiabrera *et al.*, Freestanding Perovskite Oxide Films: Synthesis, Challenges, and Properties. *Ann. Phys.,* 2200084 (2022).

30. D. Ji *et al.*, Freestanding crystalline oxide perovskites down to the monolayer limit. *Nature* **570**, 87–90 (2019).

31. G. Dong *et al.*, Super-elastic ferroelectric single-crystal membrane with continuous electric dipole rotation. *Science* **366**, 475–479 (2019).

32. S. S. Hong *et al.*, Extreme tensile strain states in $La_{0.7}Ca_{0.3}MnO_3$ membranes. *Science* **368**, 71–76 (2020).

33. R. Xu *et al.*, Strain-induced room-temperature ferroelectricity in $SrTiO_3$ membranes. *Nat. Commun.* **11**, 1-8 (2020).

34. R. Guo *et al.*, Continuously controllable photoconductance in freestanding $BiFeO_3$ by the macroscopic flexoelectric effect. *Nat. Commun.* **11**, 2571 (2020).

35. H. Elangovan *et al.*, Giant superelastic piezoelectricity in flexible ferroelectric $BaTiO_3$ membranes. *ACS nano* **14**, 5053–5060 (2020).

36. J.-K. Huang *et al.*, High-κ perovskite membranes as insulators for two-dimensional transistors. *Nature* **605**, 262–267 (2022).

37. M. Lee *et al.*, Ultrathin Piezoelectric Resonators Based on Graphene and Free-Standing Single-Crystal $BaTiO_3$. *Adv. Mater.* **34**, 2204630 (2022).

38. C. Jin *et al.*, Super-Flexible Freestanding $BiMnO_3$ Membranes with Stable

Ferroelectricity and Ferromagnetism. *Adv. Sci.* **8**, 2102178 (2021).

39. P. T. Le, J. E. Ten Elshof, G. Koster, Epitaxial lift-off of freestanding (011) and (111) $SrRuO_3$ thin films using a water sacrificial layer. *Sci. Rep.* **11**, 12435 (2021).

40. W. Zhou *et al.*, Synthesis of freestanding perovskite oxide thin films by using brownmillerite $SrCoO_{2.5}$ as a sacrificial layer. *Appl. Phys. Lett.* **122**, 062901 (2023).

41. Z. Chen *et al.*, Freestanding crystalline $YBa_2Cu_3O_{7-x}$ heterostructure membranes. *Phys. Rev. Mater.* **3**, 060801 (2019).

42. L. Gong, R. Yu, H. Ohta, T. Katayama, Synthesis and transparent conductivity of crack-free La: $BaSnO_3$ epitaxial flexible sheets. *Dalton trans.* **52**, 6317–6323 (2023).

43. P. Singh *et al.*, Large-Area Crystalline $BaSnO_3$ Membranes with High Electron Mobilities. *ACS Appl. Electron. Mater.* **1**, 1269–1274 (2019).

44. L. Gong, M. Wei, R. Yu, H. Ohta, T. Katayama, Significant Suppression of Cracks in Freestanding Perovskite Oxide Flexible Sheets Using a Capping Oxide Layer. *ACS nano* **16**, 21013–21019 (2022).

45. D. Li *et al.*, Stabilization of $Sr_3Al_2O_6$ Growth Templates for Ex Situ Synthesis of Freestanding Crystalline Oxide Membranes. *Nano Lett.* **21**, 4454–4460 (2021).

46. D. Lu *et al.*, Synthesis of freestanding single-crystal perovskite films and heterostructures by etching of sacrificial water-soluble layers. *Nat. Mater.* **15**, 1255–1260 (2016).

47. K. Gu *et al.*, Simple Method to Obtain Large-Size Single-Crystalline Oxide Sheets. *Adv. Funct. Mater.* **30**, 2001236 (2020).

48. L. Han *et al.*, Giant uniaxial strain ferroelectric domain tuning in freestanding PbTiO3 films. *Adv. Mater. Interfaces* **7**, 1901604 (2020).

49. S. R. Bakaul *et al.*, Single crystal functional oxides on silicon. *Nat. Commun.* **7**, 10547 (2016).

50. S. R. Bakaul *et al.*, High Speed Epitaxial Perovskite Memory on Flexible Substrates. *Adv. Mater. (Deerfield Beach, Fla.)* **29**, (2017).

51. D. Pesquera *et al.*, Beyond substrates: strain engineering of ferroelectric membranes. *Adv. Mater.* **32**, 2003780 (2020).

52. D. Pesquera *et al.*, Large magnetoelectric coupling in multiferroic oxide heterostructures assembled via epitaxial lift-off. *Nat. Commun.* **11**, 3190 (2020).

53. Y. Bourlier *et al.*, Transfer of epitaxial $SrTiO_3$ nanothick layers using water-soluble sacrificial perovskite oxides. *ACS Appl. Mater. Interfaces* **12**, 8466–8474 (2020).

54. H. Peng *et al.*, A Generic Sacrificial Layer for Wide-Range Freestanding Oxides with Modulated Magnetic Anisotropy. *Adv. Funct. Mater.* **32**, 2111907 (2022).

55. S. R. Bakaul *et al.*, Freestanding ferroelectric bubble domains. *Adv. Mater.* **33**, 2105432 (2021).

56. R. Takahashi, M. Lippmaa, Sacrificial Water-Soluble BaO Layer for Fabricating Free-Standing Piezoelectric Membranes. *ACS Appl. Mater. Interfaces* **12**, 25042–25049 (2020).

57. Y. Zhang *et al.*, Flexible quasi-two-dimensional $CoFe_2O_4$ epitaxial thin films for continuous strain tuning of magnetic properties. *ACS nano* **11**, 8002-8009 (2017).

58. X. Li *et al.*, Epitaxial Liftoff of Wafer-Scale VO_2 Nanomembranes for Flexible, Ultrasensitive Tactile Sensors. *Adv. Mater. Technol.* **4**, 1800695 (2019).

59. D. K. Lee *et al.*, Heterogeneous integration of single-crystalline rutile nanomembranes with steep phase transition on silicon substrates. *Nat. Commun.* **12**, 5019 (2021).

60. Y.-H. Chu, Van der Waals oxide heteroepitaxy. *npj Quantum Mater.* **2**, 67 (2017).

61. Y. Bitla, Y.-H. Chu, van der Waals oxide heteroepitaxy for soft transparent electronics. *Nanoscale* **12**, 18523–18544 (2020).

62. S. Ruppi, A. Larsson, A. Flink, Nanoindentation hardness, texture and microstructure of α-Al_2O_3 and κ-Al_2O_3 coatings. *Thin Solid Films* **516**, 5959–5966 (2008).

63. G. A. Rosales-Sosa, A. Masuno, Y. Higo, H. Inoue, Crack-resistant Al_2O_3–SiO_2 glasses. *Sci. Rep.* **6**, 1–7 (2016).

Chapter 2. Significantly Suppression of Crack in La:$SrSnO_3$ Freestanding Sheet Using an Amorphous Oxide Protection Layer

2.1. Purpose of this chapter

La:$SrSnO_3$ (LSSO) is a newly emerging perovskite material in the last decade, and attracted widespread attention owing to its wide bandgap (E_g > 4.6 eV) as well as high conductivity (> 1000 S/cm) (*1*), making it tremendous potential applications in the fields of optoelectronics and thin film transistor (*2-4*). The chemical composition of LSSO is relatively cheap and gentle to human body. The crystal structure of LSSO belongs to pseudo-double cubic perovskite ($a/2$ = 0.4034 nm) and the lattice is orthorhombic (*5*). The La^{3+} cation replaces some of the positions of Sr^{2+} cation significantly improved the electrical of the material (*6*). Although, there are many other dopants reported, such as Ta (*7*), Nb (*8*), Sb (*9*), and Nd (*9*) doped $SrSnO_3$, among them, La doped one shows higher electric property. The conduction mechanism is attribute to that the valence band maximum and conduction band minimum of $SrSnO_3$ is composed of O 2p and Sn 5s, respectively (*5*).

Energy-saving technology is essential for achieving a sustainable society. One example is light-emitting-diode (LED), which has been greatly used due to its low-cost, energy-efficient and eco-friendly since the invention of bright blue LED (*10, 11*). As vital

component of LED, transparent conductive oxides (TCOs) are widely used (*12-15*). Currently, the most used TCO is amorphous indium tin oxide (a-ITO) due to its high conductivity (>10^3 S/cm), high transparency in the visible range and easy synthesis (*16, 17*). Besides visible light, deep ultraviolet light (DUV, 200−300 nm in wavelength) is also important for sterilization and cleaning, leading to an increasing requirments of developing DUV-LED instead of traditional mercury lamp (*18, 19*). However, the bandgap of ITO (3.5 eV) is insufficient compared to the requirements of electrodes for such DUV-related devices (>4.1 eV). Hence, the demand for TCOs with high DUV transmission remains high (*20*). One promising candidate is LSSO due to the coexistence of wide bandgap and high electric conductivity. However, the film deposition temperature of LSSO, 750 °C, is too high for devices to tolerate, restricting the applications (*3, 6*).

In this chapter, I study on the significant crack suppression in the as-produced sheet via the deposition of capping oxide layers onto the objective perovskite oxide film prior to lift-off (**Figure 2-1(a)**). I systematically investigated the effects of the capping layer thickness (t_{cap}), perovskite oxide film thickness (t_{film}), and capping layer type. The results revealed that an amorphous (a-)Al_2O_3 capping layer was effective, owing to the high crack resistance and/or high Young's modulus of Al_2O_3 glass (*21*). Through this simple method, a 5 × 5 mm^2 LSSO sheet were obtained without any cracks. In addition, the LSSO sheet exhibited a wide bandgap (4.4 eV) and high electrical conductivity (>10^3 S/cm).

2.2. Experimental

Synthesis of freestanding La:$SrSnO_3$ sheet: As-grown films comprising a capping oxide/LSSO/SAO tri-layers were prepared on STO (001) single-crystal substrates using pulsed laser deposition (PLD). Three types of materials were used as capping layers, namely, an a-Al_2O_3, a-ITO, and a-TiO_2. During film growth, the substrate temperature (T_S) and oxygen pressure (P_{O2}) were maintained at 850 °C and 1×10^{-3} Pa, 750 °C and 20 Pa, and for the SAO, LSSO, and BST layers, respectively. Capping oxide layers of a-Al_2O_3, a-ITO, and a-TiO_2 were fabricated at room temperature with P_{O2} values of 1×10^{-3}, 5, and 3 Pa, respectively. The thicknesses of the capping oxide (t_{cap}), LSSO (t_{film}), and SAO layers were set to 0–1000, 30–300, and 20 nm, respectively. The as-grown films were first attached to adhesive-coated PET substrates (**Figure 2-1(b)**). The adhesive-coated PET substrates were purchased from Kimoto Co., Ltd. (Prosave™ UV). The thickness and adhesive force of the PET substrates are 100 μm and 14.8 N/25 mm, respectively. The PET/as-grown films were then placed in deionized water for 24 h to completely dissolve the SAO sacrificial layer. Although we waited for 24 h after immersing the PET/as-grown film in deionized water, 2 h might be sufficient. Subsequently, the LSSO/capping oxide/PET and BST/capping oxide/PET sheets were obtained by removing the single-crystal STO substrate (**Figure 2-1(c)**). The sheets were also prepared on glass substrates. The LSSO film grown on the STO substrate was first placed in deionized water for 2 h. After dissolving the SAO sacrificial layer, the sheet on

the STO substrate was removed from the water and then re-dropped in the deionized water. The STO substrate sank, whereas the sheet floated on the water. Finally, the floating LSSO sheet was picked up, together with the water, by the glass substrate.

***Crystallographic analyses*:** The crystal structures of the as-grown films and sheets were analyzed using high-resolution XRD (ATX-G, Rigaku Corp.), while the thicknesses of the layers were evaluated through X-ray reflectivity measurements.

***Morphology observations*:** The surface morphology was observed using AFM; Nanocute, Hitachi High-Tech Science Corp.) and SEM; SU8230, Hitachi High-Tech Science Corp.).

***Electrical conductivity measurement*:** The conductivity of the sheet was determined using the conventional four-probe DC method with a van der Pauw electrode configuration. Ga-In alloys were connected to the device with coaxial probe tips and used as the electrodes.

Optical transmittance & reflectivity measurements: Optical transmission and reflection spectra of the LSSO sheet were measured using an ultraviolet−visible−near-infrared spectrometer (UV−vis−NIR, SolidSpec-3700, Shimadzu Co.) at RT.

2.3. Result and discussion

As-grown films comprising an a-Al_2O_3 protection oxide/$La_{0.03}Sr_{0.97}SnO_3$ (LSSO)/SAO tri-layer were prepared on STO (001) single-crystal substrates. The a-Al_2O_3 layer has a flat surface and high DUV transparency (**Figure 2-2**). The thicknesses of the capping oxide (t_{cap}), LSSO (t_{film}), and SAO layers were 0–300, 30–300, and 20nm, respectively. The as-grown films were first attached to adhesive-coated PET substrates (**Figure 2-1(b)**). The PET/as-grown films were then placed in deionized water for 24 h to completely dissolve the SAO sacrificial layer. Subsequently, the LSSO/protection oxide/PET sheets were obtained by removing the single-crystal STO substrate (**Figure 2-1(c)**).

Figure 2-1(d) displays the photographs of the LSSO sheets prepared without and with the a-Al_2O_3 capping layer at a constant t_{film} value of 300 nm. Without the capping layer (t_{cap} = 0 nm), numerous cracks were generated in the sheet, resulting in a frosted glass-like appearance. By contrast, the density of cracks in the sheet significantly decreased when a capping layer was used. At t_{cap} = 10 and 30 nm, a maximum crack-free sheet area of 0.5 mm^2 was achieved, while at t_{cap} = 300 nm, no cracks were observed in the as-produced 5 × 5 mm^2 sheet. **Figure 2-1(e-f)** shows the magnified SEM images of the sheets with t_{cap} values of 0 and 300 nm. Unlike the sheet without a capping layer, there were no cracks in the sheet with the 300 nm a-Al_2O_3 capping layer, even though some pinhole structures could still be observed in the sheet (**Figure 2-1(h)**). We speculate that the pinholes are derived from a formation of droplets of SAO during the fabrication of

the as-grown film via pulsed laser deposition (PLD). In the PLD process, the PLD target (source of raw materials) is irradiated with a pulsed laser, and the raw materials are turned into plasma and supplied to the substrate. However, the raw materials reach the substrate as large particles and become droplets, even though the density is low. When the as-grown film with SAO droplets is immersed in pure water, the droplets dissolve, resulting in the formation of pinholes. These results demonstrate the usability of the capping layer for suppressing cracks in oxide sheets.

Figure 2-3(a) illustrates the out-of-plane XRD patterns of the as-grown film and LSSO (t_{film} = 300 nm) sheets using the a-Al_2O_3 protection layer as a function of t_{cap}. All the films and sheets show only intense 00*l* (*l* = 1 and 2) diffraction peaks of LSSO, indicating that the crystallographic orientation was maintained through the lift-off and transfer processes. Compared to those of the as-grown film, the XRD peaks of the sheets shifted toward the higher-angle region, indicating that the out-of-plane lattice constants (*c*) shrank after transfer. The *c*-axis length of the as-grown film was 4.036 Å, which was slightly larger than that of bulk $SrSnO_3$ (a_{bulk} = 4.034 Å), owing to the compressive strain from the SAO (*a*/4 = 3.961 Å) layer. Upon removing the SAO layer, *c* decreased to 4.034 Å, which was the same as a_{bulk}, owing to the release of compression strain from SAO (**Figure 2-4)**.

Figure 2-3(b) shows the RSM of the as-grown film (t_{film} = 300 nm) with an a-Al_2O_3 capping layer (t_{cap} = 300 nm). The 40$\underline{12}$ SAO and 103 LSSO diffraction spots appeared near the 103 STO diffraction spot. The in-plane lattice constant of the SAO layer (0.392 nm) was slightly lower than the out-of-plane lattice constant (0.397 nm) because

of the compressive strain from the STO substrate (a = 0.3905 nm). Moreover, the 103 LSSO diffraction intense spots comprised strong and weak streaks corresponding to the unstrained and strained lattices, respectively, which may be due to the strain relaxation when the film thickness exceeded the critical thickness. The unstrained lattice had near-identical in-plane and out-of-plane lattice constants. By contrast, the in-plane lattice constant of the strained lattice differed from the out-of-plane one, which were 0.397 and 0.410 nm, respectively, in the as-grown film. The volume fraction of the strained lattices was determined from the peak intensity ratio to be 5.5%. After dissolving the SAO layer (**Figure 2-3(c)**), the peak from the strained lattices became weaker, owing to the release of compressive strain from the SAO layer. However, a peak from the strained lattices was still observed, even though the volume fraction of the strained lattices was only 0.3%. These results suggest that although the compressive strain became significantly weaker, it was still present because of the strain from the capping a-Al_2O_3 layer. The full width at half maximum of the rocking curve for the 002 peak of the sheet was 0.7°, which is slightly larger than that of the as-grown film (0.5°; **Figure 2-3(d)**). The sheet displayed a flat surface with a root mean square value of roughness of 0.2 nm (**Figure 2-3(e)**).

Next, we elucidated the effect of t_{film} on crack generation in the sheets. **Figure 2-5(a, b)** displays photographs of the sheets comprising a-Al_2O_3 capping layers (t_{cap} = 300 nm) with t_{film} values of 30 and 100 nm. In contrast to the sheet with a t_{film} value of 300 nm (**Figure 2-1(d)**), sheets with t_{film} values of 30 and 100 nm presented some wrinkles; however, no marked cracks were observed in the sheets. **Figure 2-5(c, d)** illustrates the

a- and *c*-axis lengths of the as-grown films and sheets, respectively, as a function of t_{film}. For the as-grown films, the lattice constants approached those of the bulk with increasing t_{film}. Such behavior is also observed in the La-doped $BaSnO_3$ film because the in-plane lattice constant of the film relaxes with increasing distance from the substrate owing to the presence of dislocations in the film (*22*). After removing the SAO layer, the *c*- and *a*-axis lengths approached the a_{bulk} value, owing to the release of the compressive strain from the SAO layer. The observed changes in the *c*-axis lengths before and after the transfer were –0.54%, –0.62%, and –0.15% for t_{film} values of 30, 100, and 300 nm, respectively. Thus, we concluded that the wrinkles in the sheets with smaller t_{film} values are derived from the large change in the lattice constants before and after the transfer.

In the aforementioned experiment, an adhesive-coated PET substrate was used for the transfer, as illustrated in **Figure 2-1**. We next investigated the effect of solely placing the as-grown film in deionized water (**Figure 2-6(a, b)**). **Figure 2-6(e)** displays a photograph of the as-grown film (t_{film} = 300 nm and t_{cap} = 300 nm) immediately after it was placed without the PET substrate in deionized water. After 10 mins, the SAO layer dissolved slightly from the edges and some of the center points of the film, suggesting that pinholes in the film allowed water to infiltrate it. Clearly, the SEM images (**Figure 2-1(h)**) show the presence of pinholes in the LSSO sheet. The SAO layer was completely dissolved after 60 mins, and no cracks were observed in the sheet. Notably, the LSSO sheet rolled spontaneously. This was attributed to the larger in-plane length of the LSSO sheet compared to that of the as-grown film, owing to the compressive strain release following

the removal of the SAO layer, while that of the a-Al_2O_3 capping layer remained unchanged. The rolled sheet was placed onto the STO substrate through van der Waals forces (**Figure 2-6(b)**). After re-dipping the STO substrate in deionized water, the rolled sheet floated on the water and was picked and transferred onto a glass substrate (**Figure 2-6(c)**). **Figure 2-6(f)** presents a photograph of the sheet after the transfer. The sheet on the glass substrate could be rolled and unrolled repeatedly through mechanical forces, such as airflow generated by a washing ear ball and/or manual vibration (**Figure 2-6(d, g)**), demonstrating the excellent flexibility and elasticity of the sheet. Notably, when the sheet was transferred onto other substrates, we could select whether the LSSO layer in the sheet was the upper or lower layer by changing the transfer method (**Figure 2-7**). Such large LSSO sheets could not be obtained without a capping oxide layer.

We also tested other capping oxide layers, namely, a-TiO_2 and a-ITO. **Figure 2-8** displays a photograph of the LSSO (t_{film} = 300 nm) sheets fabricated using these capping layers. When an a-TiO_2 capping layer was used, numerous cracks were generated in the sheet. By contrast, crack generation was suppressed when the a-ITO capping layer was used. However, the a-Al_2O_3 capping layer was more effective in suppressing crack generation. Al_2O_3 has both high hardness and toughness (*23*). Because of this, for example, in SiO_2-Al_2O_3 glass, high crack resistance is achieved by increasing the Al_2O_3 content (*21*). We speculate that the superior results of the a-Al_2O_3 capping layer are derived from the high crack resistance of Al_2O_3 glass. Another possibility is that the high Young's modulus of Al_2O_3 plays an important role in preventing the formation of cracks in the

sheet. The Young's modulus of Al_2O_3 (~340 GPa) is much higher than those of ITO (~190 GPa) and TiO_2 (~65-150 GPa) (*24-26*).

The inset in **Figure 2-9(a)** illustrates the optical transmission (*T*) and reflection (*R*) spectra of the LSSO sheet transferred onto the glass substrate. The *T* value was 65% at 4.1 eV, even for a thick sheet (LSSO layer, 300 nm), indicating great potential for DUV transparent applications. The optical bandgap was evaluated using a Tauc plot from the $(\alpha hv)^2$–hv curve (**Figure 2-9(a)**), where α denotes the absorption coefficient and hv is the photon energy, assuming direct transition. The optical bandgap was 4.4 eV, which is slightly smaller than that observed for Ta-doped $SrSnO_3$, Nb-doped $SrSnO_3$, and LSSO films on MgO substrates (~4.6 eV) (*7, 8*). **Figure 2-9(b)** shows the electrical conductivity (σ) of the LSSO sheet as a function of temperature. The value of σ increases with decreasing *T*, indicating that the LSSO sheet is a degenerate semiconductor, similar to LSSO films (*3*). The σ of the sheet was 1.6×10^3 S/cm at room temperature, which is slightly lower than that of the LSSO film on the STO substrate (3×10^3 S/cm), but similar to that of a-ITO (2×10^3 S/cm) (*27*).

Figure 2-9(c) shows room-temperature σ against the optical bandgap for various oxides that can be prepared at room temperature on amorphous substrates. The circular marks represent oxides fabricated directly on the substrates, such as a-ITO (*27*), amorphous indium gallium zinc oxide (a-IGZO) (*28*), and Al-doped ZnO (*29*), while the triangular marks correspond to oxides obtained through lift-off and transfer techniques, including La-doped $BaSnO_3$ and as-produced LSSO sheets (*30*). Notably, the optical bandgap of

the LSSO sheet (4.4 eV) was within the DUV region and significantly wider than those of conventional transparent conductive oxides (<3.5 eV at σ > 10 S/cm). In addition, the σ value of the LSSO sheet (1.6×10^3 S/cm) was higher than those of the other oxides. These results demonstrate the significant potential of the LSSO sheet as a DUV transparent electrode.

2.4. Conclusion

We demonstrated that the generation of cracks can be significantly suppressed in freestanding sheets using a capping oxide layer. LSSO were obtained with crack-free areas as large as 5 × 5 mm^2, using a simple method. When the sheets were transferred onto other substrates, we could select the objective layer in the sheets to be the upper or lower layer. The LSSO sheet exhibited a much wider optical bandgap of 4.4 eV than other transparent conductive oxides and a high σ value of 1.6×10^3 S/cm at room temperature. Additionally, the high-cost $SrTiO_3$ single-crystal substrates are reusable. In conclusion, our findings provide a simple transfer method for obtaining large-size, high-quality single-crystalline sheets on arbitrary substrate.

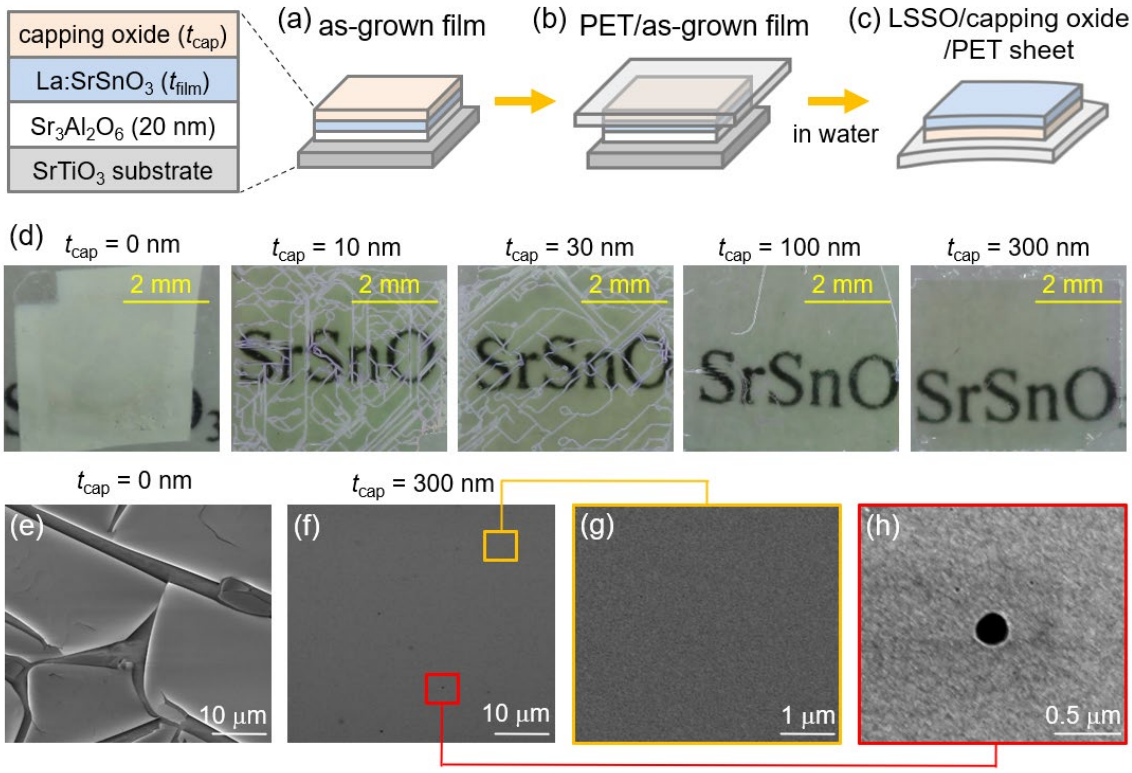

Figure 2-1. Synthesis and transfer of LSSO sheet. Schematics of the (a) as-grown film, (b) PET/as-grown film, and (c) LSSO/capping oxide/PET sheet. The thickness of the capping oxide and LSSO layers are labeled t_{cap} and t_{film}, respectively. (d) Photograph of the obtained LSSO (t_{film} = 300 nm) sheets using a-Al_2O_3 capping layers as a function of t_{cap}. Scanning electron microscopy (SEM) images of LSSO sheets (e) without the capping oxide layer and (f, g, h) with the 300 nm a-Al_2O_3 capping layer.

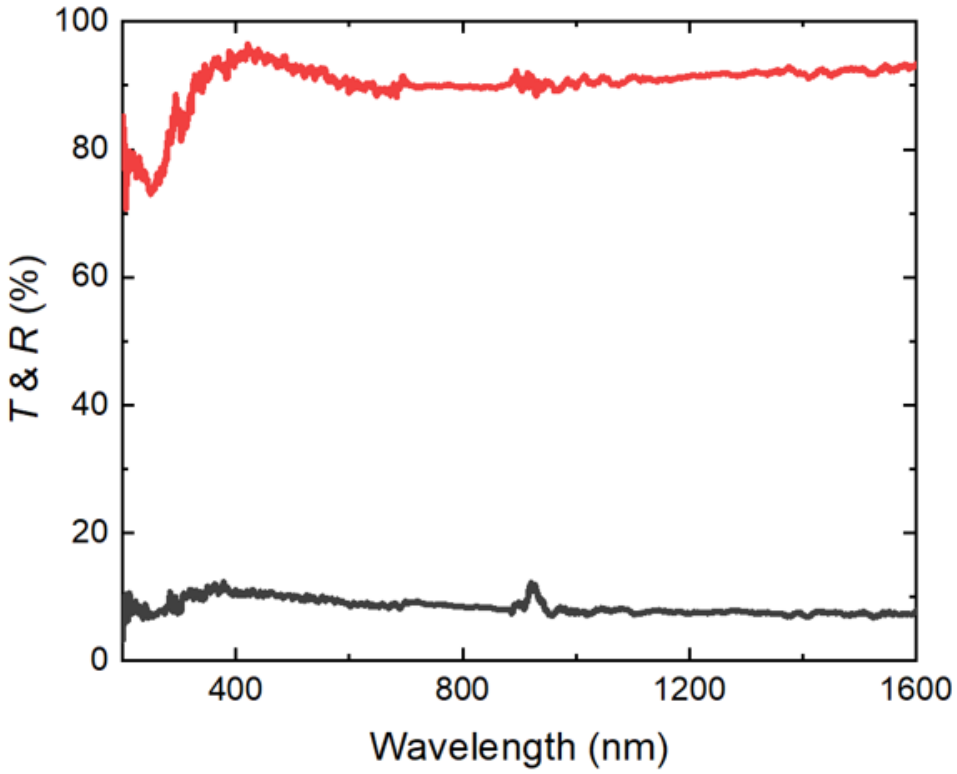

Figure 2-2. Optical property of a-Al_2O_3 protection layer. Transmitta0nce and reflectivity of 100 nm-thick a-Al_2O_3 film on SiO_2 glass substrate.

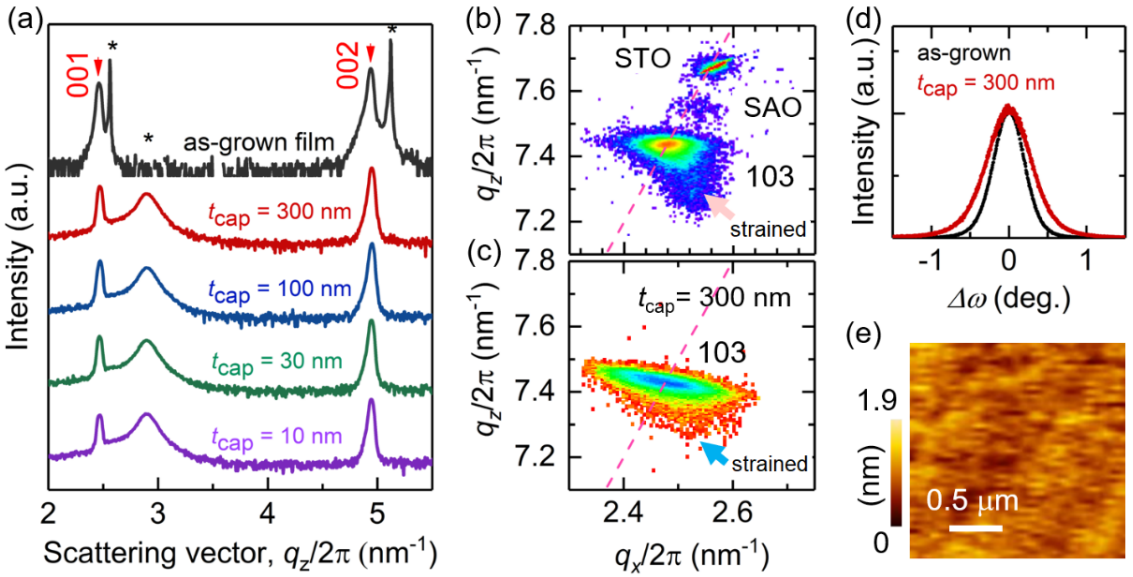

Figure 2-3. Charactrization of LSSO sheet. (a) Out-of-plane X-ray diffraction (XRD) patterns for the as-grown and LSSO sheets as a function of t_{cap}. (b) Reciprocal space mapping (RSM) of the as-grown film and (c) RSM, (d) rocking curves, and (e) atomic force microscopy (AFM) image of the sheet with a t_{cap} value of 300 nm. The sheets (t_{film} = 300 nm) were prepared using a-Al_2O_3 capping layers. Asterisks correspond to the STO or PET substrates.

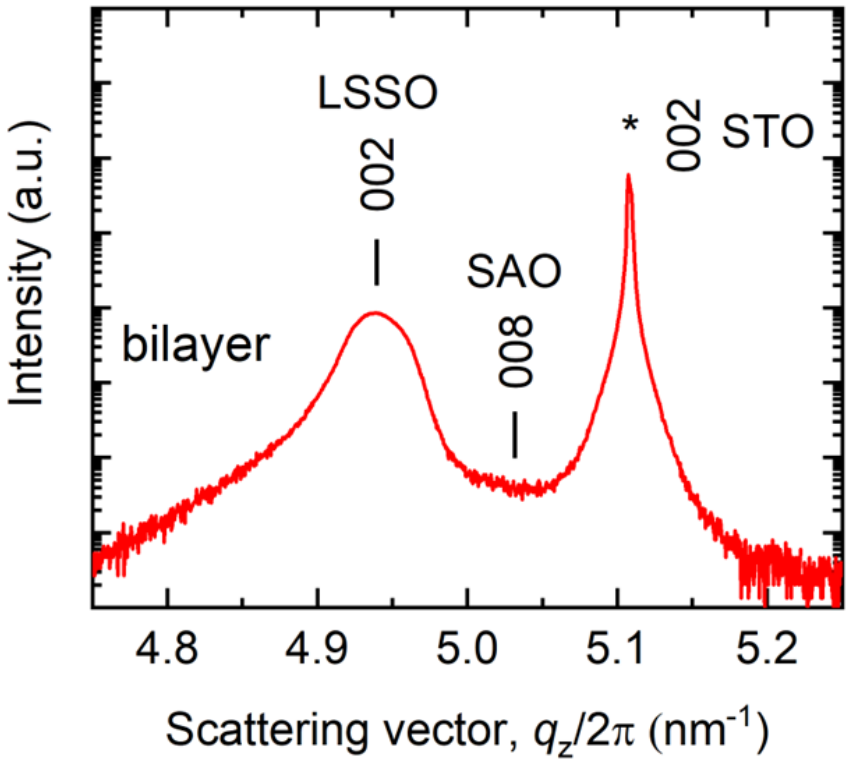

Figure 2-4. XRD patten for the as-grown LSSO film. Asterisks correspond to the STO substrates.

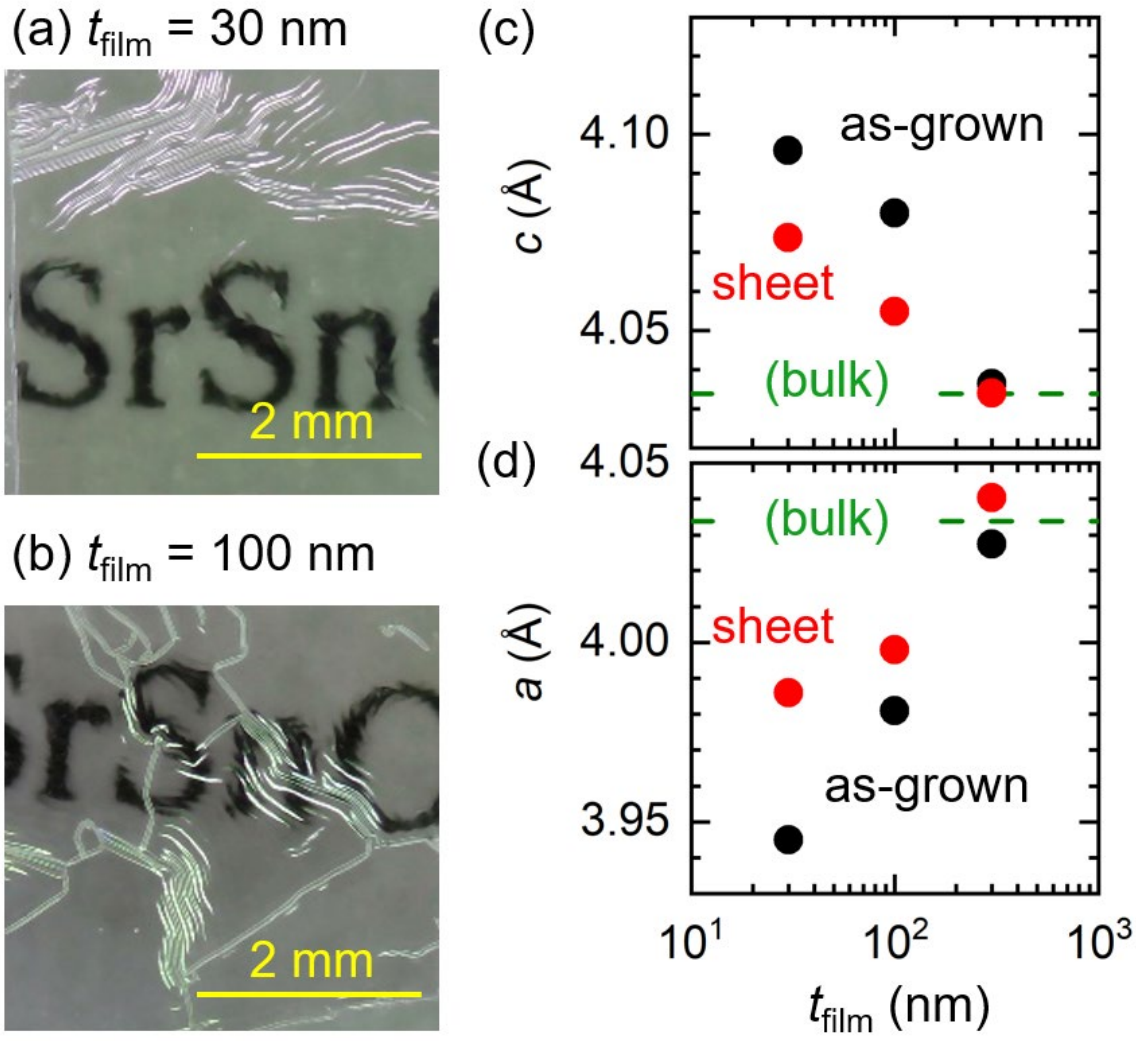

Figure 2-5. Film thickness dependence of LSSO sheet. Photographs of the LSSO sheets for t_{film} = (a) 30 and (b) 100 nm using a-Al_2O_3 capping layers (t_{cap} = 300 nm) and (c) *c*- and (d) *a*-axis lengths of the as-grown films and sheets (t_{cap} = 300 nm) as a function of t_{film}. The green dotted line indicates the *a*-axis length of bulk cubic $SrSnO_3$.

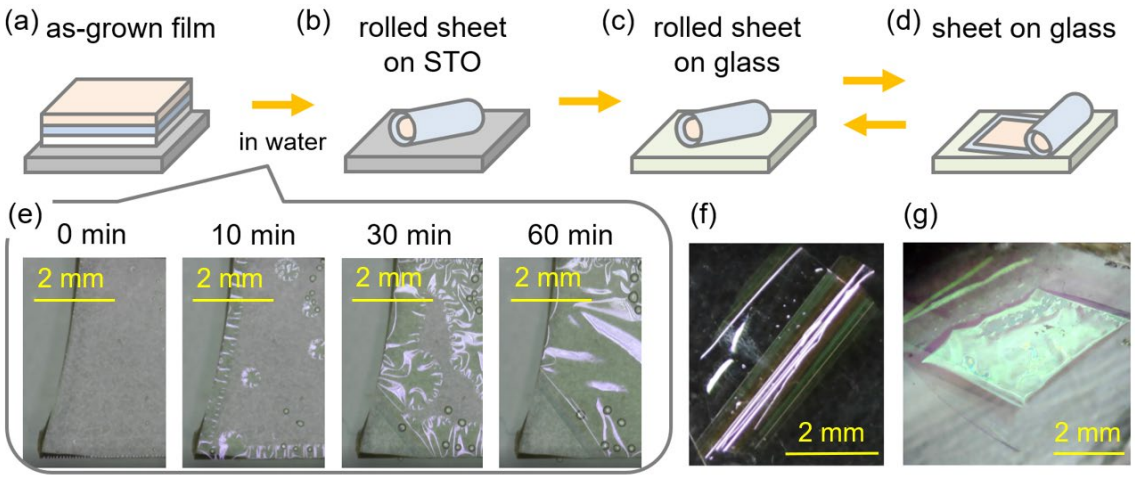

Figure 2-6. Transfer of freestanding LSSO sheet. Schematics of the (a) as-grown film, (b) rolled film on STO, (c) rolled film on glass, and (d) spread film on glass. (e) Time-lapse photographs of the as-grown film directly immersed into deionized water. Photograph of (f) rolled film and (g) spread film on glass.

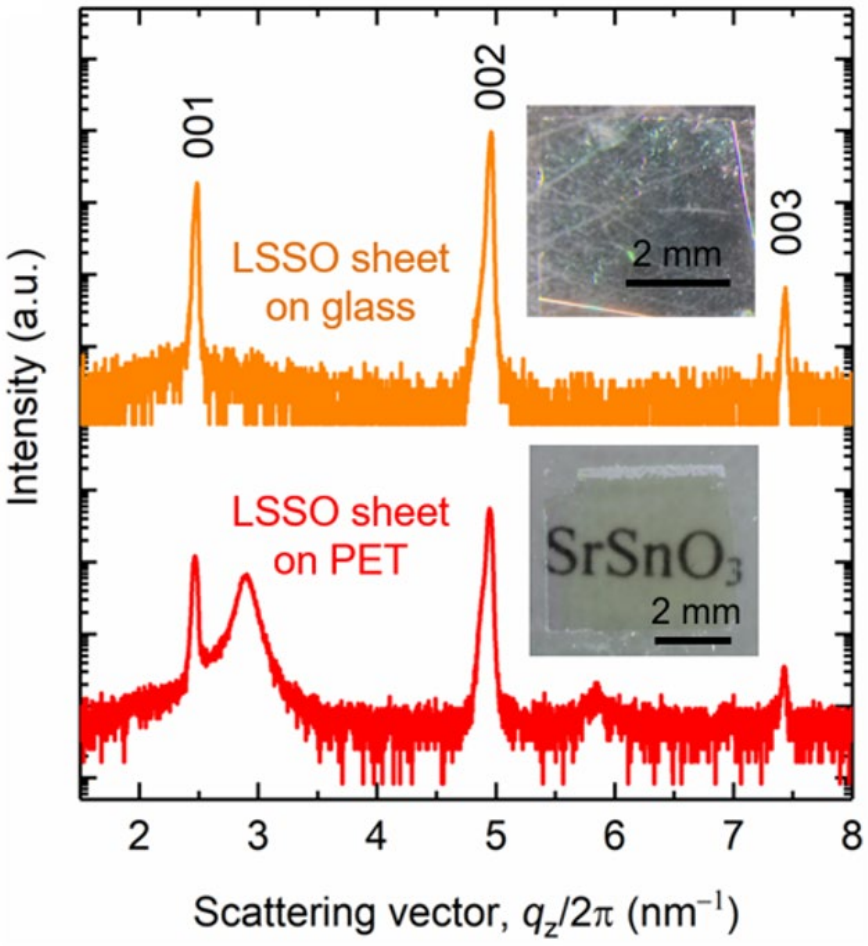

Figure 2-7. XRD pattern of LSSO sheet on glass. Out-of-plane XRD patterns of the LSSO sheets on glass (orange) and PET (red) substrates.

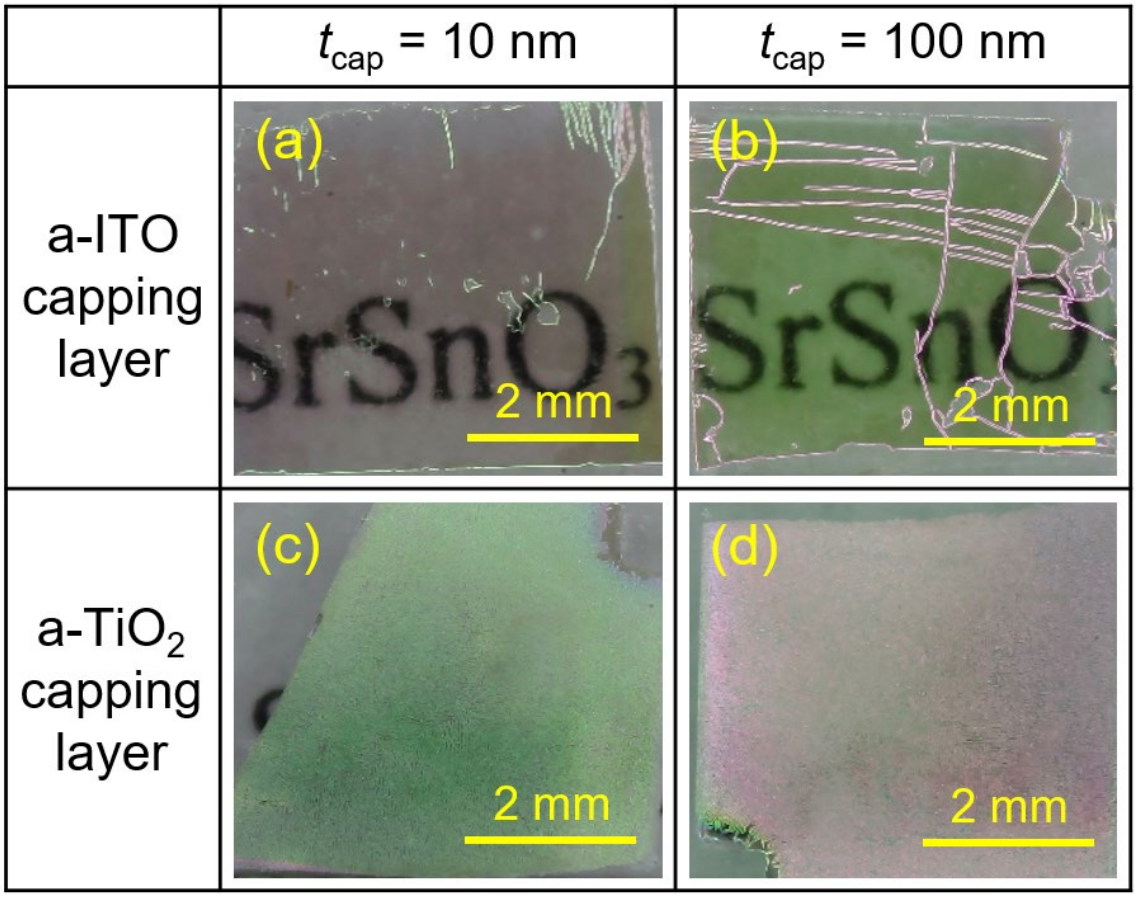

Figure 2-8. Photograph of using a-ITO and a-TiO$_2$ protection layer. Photographs of the LSSO sheets by comprising a-ITO capping layers with t_{cap} of (a) 10 and (b) 100 nm and a-TiO$_2$ capping layers with t_{cap} of (c) 10 and (d) 100 nm. t_{film} = 300 nm.

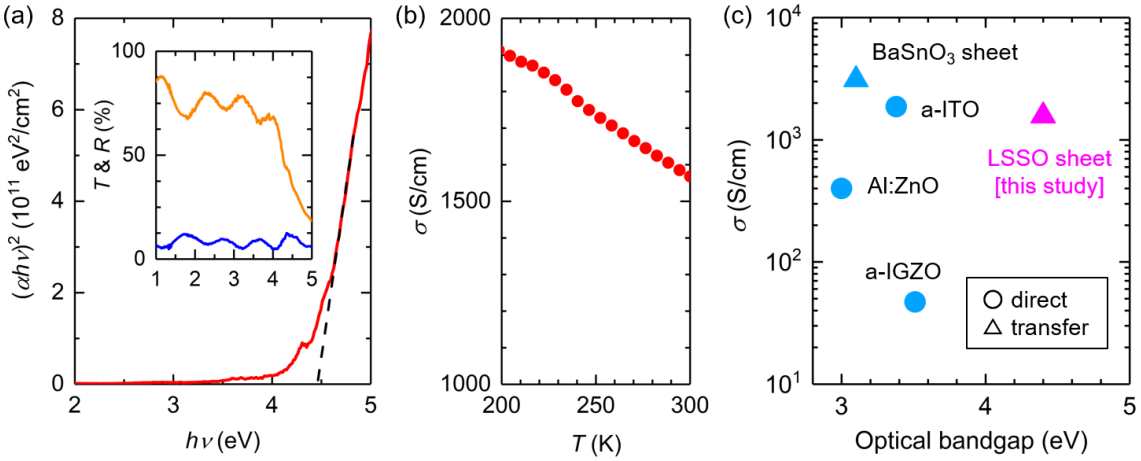

Figure 2-9. Optical and conductivity of LSSO sheet. (a) Photon energy dependence of $(\alpha hv)^2$ and (b) temperature dependence of the electrical conductivity for the LSSO sheet transferred onto the SiO_2 glass substrate; inset in (a) shows the transmittance and reflectance. (c) Room-temperature electrical conductivity against the optical bandgap for various oxides that can be prepared at room temperature on amorphous substrates.

References

1. E. Baba *et al.*, Optical and transport properties of transparent conducting La-doped $SrSnO_3$ thin films. *J. Phys. D: Appl. Phys.* **48**, 455106 (2015).

2. J. Seo, J. Kim, J. H. Kim, J. H. Kim, K. Char, Fully Deep‐UV Transparent Thin Film Transistors Based on $SrSnO_3$. *Adv. Electron. Mater.*, 2300547 (2023).

3. M. Wei, L. Gong, D. d. Liang, H. J. Cho, H. Ohta, Fabrication and Operating Mechanism of Deep‐UV Transparent Semiconducting $SrSnO_3$‐Based Thin Film Transistor. *Adv. Electron. Mater.* **6**, (2020).

4. V. S. K. Chaganti, A. Prakash, J. Yue, B. Jalan, S. J. Koester, Demonstration of a depletion-mode $SrSnO_3$ n-channel MESFET. *IEEE Electron Device Lett.* **39**, 1381-1384 (2018).

5. E. Moreira *et al.*, Structural, optoelectronic, infrared and Raman spectra of orthorhombic $SrSnO_3$ from DFT calculations. *J. Solid State Chem.* **184**, 921-928 (2011).

6. M. Wei *et al.*, High electrical conducting deep-ultraviolet-transparent oxide semiconductor La-doped $SrSnO_3$ exceeding~ 3000 S cm^{-1}. *Appl. Phys. Lett.* **116**, 022103 (2020).

7. Q. Liu, F. Jin, G. Gao, W. Wang, Ta doped $SrSnO_3$ epitaxial films as transparent conductive oxide. *J. Alloys Compd.* **717**, 62-68 (2017).

8. K. Li, Q. Gao, L. Zhao, Q. Liu, Electrical and Optical Properties of Nb-doped $SrSnO_3$ Epitaxial Films Deposited by Pulsed Laser Deposition. *Nanoscale Res. Lett.* **15**, 164 (2020).

9. Q. Liu *et al.*, Perovskite-type transparent and conductive oxide films: Sb-and Nd-doped $SrSnO_3$. *Thin Solid Films* **519**, 6059-6063 (2011).

10. Y. Nanishi, The birth of the blue LED. *Nat. Photonics* **8**, 884-886 (2014).

11. S. Nakamura, The roles of structural imperfections in InGaN-based blue light-emitting diodes and laser diodes. *Science* **281**, 956-961 (1998).

12. H. Hosono, K. Ueda, Transparent conductive oxides. *Springer handbook of electronic and photonic materials*, 1-1 (2017).

13. A. Prakash, B. Jalan, Wide Bandgap Perovskite Oxides with High Room - Temperature Electron Mobility. *Adv. Mater. Interfaces* **6**, 1900479 (2019).

14. H. Ohta, H. Hosono, Transparent oxide optoelectronics. *Mater. Today* **7**, 42-51 (2004).

15. S. Kasap, P. Capper, *Springer handbook of electronic and photonic materials*. (Springer, 2017).

16. H. Morikawa, M. Fujita, Crystallization and electrical property change on the annealing of amorphous indium-oxide and indium-tin-oxide thin films. *Thin Solid Films* **359**, 61-67 (2000).

17. J. Bellingham, W. Phillips, C. Adkins, Electrical and optical properties of amorphous indium oxide. *J. Phys.: Condens. Matter* **2**, 6207 (1990).

18. W. Zheng *et al.*, Vacuum-ultraviolet photovoltaic detector. *Acs Nano* **12**, 425-431 (2018).

19. Z. Zhang *et al.*, A 271.8 nm deep-ultraviolet laser diode for room temperature operation. *Applied Physics Express* **12**, 124003 (2019).

20. J. C. Sutherland, K. P. Griffin, Absorption spectrum of DNA for wavelengths greater than 300 nm. *Radiat. Res.* **86**, 399-410 (1981).

21. G. A. Rosales-Sosa, A. Masuno, Y. Higo, H. Inoue, Crack-resistant Al_2O_3–SiO_2 glasses. *Sci. Rep.* **6**, 1-7 (2016).

22. H. Yun, A. Prakash, T. Birol, B. Jalan, K. A. Mkhoyan, Dopant Segregation Inside and Outside Dislocation Cores in Perovskite $BaSnO_3$ and Reconstruction of the Local Atomic and Electronic Structures. *Nano Lett.* **21**, 4357-4364 (2021).

23. S. Ruppi, A. Larsson, A. Flink, Nanoindentation hardness, texture and microstructure of α-Al_2O_3 and κ-Al_2O_3 coatings. *Thin Solid Films* **516**, 5959-5966 (2008).

24. S. Davis, G. Gutiérrez, Structural, elastic, vibrational and electronic properties of amorphous Al_2O_3 from ab initio calculations. *J. Phys.: Condens. Matter* **23**, 495401

(2011).

25. B.-K. Lee, Y.-H. Song, J.-B. Yoon, in *2009 IEEE 22nd International Conference on Micro Electro Mechanical Systems*. (IEEE, 2009), pp. 148-151.

26. O. Anderson, C. Ottermann, R. Kuschnereit, P. Hess, K. Bange, Density and Young's modulus of thin TiO_2 films. *Fresenius' journal of analytical chemistry* **358**, 315-318 (1997).

27. V. Teixeira, H. Cui, L. Meng, E. Fortunato, R. Martins, Amorphous ITO thin films prepared by DC sputtering for electrochromic applications. *Thin Solid Films* **420**, 70-75 (2002).

28. M. Orita, H. Ohta, M. Hirano, S. Narushima, H. Hosono, Amorphous transparent conductive oxide InGaO3 (ZnO) m (m≦ 4): a Zn4s conductor. *Philos. Mag. B* **81**, 501-515 (2001).

29. S. Cornelius *et al.*, Achieving high free electron mobility in ZnO: Al thin films grown by reactive pulsed magnetron sputtering. *Appl. Phys. Lett.* **94**, 042103 (2009).

30. P. Singh *et al.*, Large-Area Crystalline $BaSnO_3$ Membranes with High Electron Mobilities. *ACS Appl. Electron. Mater.* **1**, 1269-1274 (2019).

Chapter 3. Transfer of Large-area Crack-free La:$BaSnO_3$ Epitaxial Flexible Sheet Using Amorphous Al_2O_3 Protection Layer

3.1. Purpose of this chapter

La:$BaSnO_3$ (LBSO) is also newly emerging perovskite material in the last decade, and attracted widespread attention owing to its wide bandgap (E_g > 3.1 eV) and high significantly high electron mobility conductivity (320 $cm^2 V^{-1} s^{-1}$) in single-crystal form (*1*), making it high potential applications in fabrication of high photovoltaic conversion efficiency solar cell (*2-4*), transparent thin film with high conductivity (*5*), and high electron mobility transistor (*6*). The crystal structure of $BaSnO_3$ belongs to cubic perovskite (a = 0.4116 nm) (*7*). The La doping contributes to the high carrier concentration (*8*). In addition, the conduction mechanism of LBSO is also similar with LSSO that the valence band maximum and conduction band minimum of $BaSnO_3$ is composed of O 2p and Sn 5s, respectively.

The development of flexible materials with high transparency and conductivity is crucial for next-generation optoelectronic applications such as wearable devices. Conventional flexible transparent conductive materials are mainly limited to ultra-thin metals (*9*), nanocarbons (carbon nanotubes and graphene) (*10-12*), conductive polymers (*13*), and amorphous oxide semiconductors (*14-16*). However, the investigation of

crystallized oxides with high orientation is also important to utilize their unique functionalities such as high Hall mobility. I focused on crystallized LBSO, owing to its outstanding transparent conductivity. Additionally, because LBSO does not contain rare elements such as indium and it is stable against high temperatures and humidity. Although flexible amorphous LBSO films do not exhibit high electrical conductivity, I expected that the epitaxial LBSO sheet, which is peeled off and transferred on a flexible substrate, would simultaneously exhibit high electrical conductivity and flexibility.

In this chapter, I demonstrate the fabrication of crack-free large-size LBSO sheets with high crystallinity and high orientation through the lift-off and transfer method using SAO and a-Al_2O_3 as sacrificial and protection layers, respectively. Two types of LBSO sheets, rolled and flat, were obtained. The rolled sheet had a tubular shape with a height of 5 mm and a diameter of 1 mm, whereas the lateral size of the flat sheet was 5 mm × 5 mm. A significantly large crack-free area was achieved owing to the use of an a-Al_2O_3 protection layer. The difference in curvature between the rolled and flat sheets was as large as 2 mm^{-1}, indicating a high potential for flexible applications of LBSO sheets. LBSO sheets exhibit a wide optical bandgap (3.5 eV) and a higher Hall mobility (80 $cm^2 V^{-1} s^{-1}$) than other transparent conducting oxide (TCO) films grown on glass, such as indium tin oxide (ITO) (*15*), Al-doped ZnO (*16*), and F-doped SnO_2 (*14*).

3.2. Experimental

Synthesis of freestanding La:$BaSnO_3$ sheet: The as-grown films consisting of a-Al_2O_3/LBSO/SAO trilayers were first deposited on $SrTiO_3$(001) single-crystal substrates through pulsed laser deposition (PLD). As the PLD target of the LBSO layer, a $La_{0.02}Ba_{0.98}SnO_{3-\delta}$ ceramic target was synthesized by pre-sintering a mixture of La_2O_3, $BaCO_3$, and SnO_2 powders at 1350 ℃ and sintering the pellet at 1400 ℃. The SAO ceramic target was synthesized by pre-sintering a mixture of $SrCO_3$ and Al_2O_3 powders at 1350 ℃ and sintering the pallet at 1350 ℃. During film deposition, the substrate temperature, oxygen pressure, laser fluence, and laser frequency were precisely controlled at 850 ℃, 10^{-3} Pa, 0.5 J cm^{-2} $pulse^{-1}$, and 2 Hz for the SAO layer; 750 ℃, 20 Pa, 2 $Jcm^{-2}pulse^{-1}$, and 10 Hz for the LBSO layer; and room temperature, 10^{-3} Pa, 2 $Jcm^{-2}pulse^{-1}$, and 10 Hz for the a-Al_2O_3 layer, respectively. The thicknesses of the a-Al_2O_3, LBSO, and SAO layers were 300, 300, and 20 nm, respectively. The a-Al_2O_3/LBSO layers were peeled from the STO substrate by dissolving the SAO layer in pure water. The as-grown films were placed in pure water for 24 h using two different methods, as illustrated in **Figure 3-1**. In the first method, the as-grown film was immersed in pure water with the substrate side facing down. In the second method, the surface of the as-grown film was attached to an adhesive-coated polyethylene terephthalate (PET) substrate before being immersed in pure water. Thereafter, the as-grown PET-attached film was immersed in pure water. Adhesive-coated PET substrates were purchased from

Kimoto Co., Ltd. (Prosave UV). The thickness and adhesive force of the PET substrates were 100 μm and 14.8 N/25 mm, respectively.

***Crystallographic analyses*:** The crystal structures of the as-grown films and obtained sheets were evaluated using X-ray diffraction (XRD) measurements (ATX-G, Rigaku Co.), while the thicknesses of the layers were evaluated through X-ray reflectivity measurements.

***Morphology observations*:** The surface morphology of the sheets was determined through atomic force microscopy (AFM) measurements (Nanocute, Hitachi High-Tech Science Corp.).

***Electrical conductivity & Hall mobility measurements*:** The conductivity and Hall mobility of the sheets were determined using the conventional four-probe DC method with a van der Pauw electrode configuration.

Optical transmittance & reflectivity measurement: Optical transmission and reflection spectra of the LSSO sheet were measured using an ultraviolet−visible−near-infrared spectrometer (UV−vis−NIR, SolidSpec-3700, Shimadzu Co.) at RT.

3.3. Result and discussion

The as-grown film of the a-Al_2O_3/LBSO/SAO tri-layer was immersed in pure water with the substrate side facing down for 24 h (**Figure 3-1(b)**). The SAO layer started to dissolve in pure water from the edge and completely dissolved after approximately 2 h. Thereafter, the a-Al_2O_3/LBSO bi-layer was peeled off from the substrate and rolled spontaneously in pure water (**Figure 3-1(c)**). Hereafter, the bi-layer sheet is referred to as a LBSO sheet. The rolled LBSO sheet was still attached to the STO substrate owing to van der Waals forces. When the substrate was picked from pure water using tweezers without turning it upside down, the rolled LBSO sheet could also be picked up together with the substrate (**Figure 3-1(d)**). The rolled LBSO sheet can be transferred to other substrates such as glass using a sharp needle and tweezers as follows (**Figure 3-1(e)**): (1) stick the needle into the hole of the rolled LBSO sheet, (2) lift it up, (3) move it on another substrate, and (4) pull the needle out of the hole of the rolled sheet. **Figure 3-2(a)** shows the top and lateral views of the rolled LBSO sheet transferred onto glass. The rolled LBSO sheet had a tubular shape with a height of 5 mm and a diameter of 1 mm. The curvature of the rolled LBSO sheet was as large as 2 mm^{-1}, which is significantly larger than that previously reported for LBSO (*17*). The surface of the tube is an LBSO layer. The tubular shape of the rolled LBSO sheet indicates that the in-plane lattice constant of the LBSO layer increased upon the removal of the SAO layer.

A flat LBSO sheet was also prepared. **Figures 3-1(f–g)** illustrate the synthesis of the

flat sheet. The surface of the as-grown film was first attached to an adhesive-coated PET substrate (**Figure 3-1(f)**). Thereafter, the PET-attached as-grown film was immersed in pure water for 24 h. After the SAO sacrificial layer was dissolved in pure water, the STO substrate was peeled from the surface of the sheet. The LBSO sheet remained flat on the PET substrate (**Figure 3-1(g)**) because the adhesive force of the PET substrate was significantly stronger than the van der Waals force between the sheet and STO substrate. **Figure 3-2(b)** shows a photograph of the flat LBSO sheet on the PET substrate. No cracks were observed on the sheet. A. Gustavo *et al* reported high crack resistance properties of Al_2O_3-containing glasses (*18*). They fabricated $_xAl_2O_{3(1-x)}SiO_2$ glasses (x = 0.3–0.6) and found that the glass cracking resistance increased with increasing x; especially, the x = 0.6 glass exhibited the highest indentation cracking resistance, elastic moduli, and hardness in the binary system (*18*). The authors proposed that the local structure around aluminum atoms play a key role in the increased cracking resistance through shear deformation processes (*18*). In this study, we further increased the aluminum content and used a-Al_2O_3 as protection layer, resulting in crack-free LBSO sheet. The lateral size of the sheet was 5 mm × 5 mm, which was larger than that of a previously reported LBSO sheet (2 mm × 5 mm) (*17*).

Figure 3-3(a) shows the out-of-plane XRD pattern of the as-grown films. The 001 and 002 diffraction peaks of LBSO were clearly observed along with the 008 diffraction peak of SAO (inset of **Figure 3-3(a)**). The full width half maximum of the rocking curve for the SAO 008 diffraction peak is 2.8° (**Figure 3-4**). The SAO 008 diffraction peak was

observed at $q_z/2\pi = 5.06$ nm^{-1} in the out-of-plane XRD pattern (**Figure 3-3(a)**). **Figure 3-4(a)** shows rocking curves at $q_z/2\pi = 5.06$ nm^{-1} for the as-grown film grown on STO substrate and only STO substrate. In both samples, sharp STO 002 diffraction peaks were observed. Compared to the only STO substrate, the as-grown film shows a wide shoulder in the rocking curve. **Figure 3-4(b)** shows the result of fitting a rocking curve of the as-grown film contains two peaks. The sharp peak is derived from STO 002 diffraction peak, while the narrow peak originates from the SAO 008 diffraction peak. The full width half maximum of the rocking curve for the SAO 008 diffraction peak is 2.8°.

Figure 3-5 shows the reciprocal space map (RSM) around the STO 103 diffraction peak of the as-grown film. **Figure 3-5(b)** shows the result of fitting a rocking curve of the as-grown film contains two peaks. The sharp peak is derived from STO 002 diffraction peak, while the narrow peak originates from the SAO 008 diffraction peak. The full width half maximum of the rocking curve for the SAO 008 diffraction peak is 2.8°. A spot-like 103 diffraction peak was also observed for LBSO. These results indicate that the LBSO layer was hetero-epitaxially grown on the SAO layer. This is because the crystal structure of SAO, particularly the arrangement of Sr ions, is similar to that of the perovskite structure, as illustrated in **Figure 3-1**. The in-plane and out-of-plane lattice constants (*a* and *c*, respectively) of the LBSO layer in the as-grown film were determined as 4.11 and 4.135 Å, respectively. In comparison with bulk $BaSnO_3$ ($a = 4.116$ Å) (*5*), the LBSO layer in the as-grown film has a shorter *a* but longer *c*, indicating that the LBSO layer is under compressive strain from the SAO layer. This is reasonable because *a*/4 of bulk SAO (*a*/4

= 3.961 Å) is shorter than the *a* of bulk $BaSnO_3$. As shown in **Figure 3-2(a)**, the tubular shape of the rolled LBSO sheet indicates that the in-plane lattice constant of the LBSO layer increased upon the removal of the SAO layer. The increase in the in-plane lattice constant is due to the release of the compressive strain in the LBSO layer by peeling off from the SAO/STO substrate.

Figure 3-3(b) shows the out-of-plane XRD pattern of the flat LBSO sheet on PET. The 001 and 002 diffraction peaks of LBSO were still observed, indicating that the crystallographic orientation was maintained throughout the sheet synthesis process. However, the 008 diffraction peak of SAO disappeared because the SAO layer dissolved in pure water. The 001 and 002 diffraction peaks of LBSO shifted to the higher-angle side, whereas the *c* value decreased to 4.123 Å. This is derived from the release of in-plane compressive lattice strain from the substrate by removing the SAO layer. The intensity ratio of the 001 to 002 diffraction peaks of the flat LBSO sheet was 0.84%, which is almost equal to that of bulk $BaSnO_3$ (1.2%) and the as-grown film (0.96%) (**Figure 3-3(a)**).

The crystallinity of the flat LBSO sheet was evaluated using rocking curve measurements of the 002 diffraction peaks (**Figure 3-6(a)**). The full width at half maximum of the rocking curve was 0.6°, which was wider than that of the as-grown film (0.2°), indicating that crystallinity decreased during the sheet synthesis process. We speculate that the in-plane lattice constant of the LBSO layer increases slightly owing to the release of the in-plane compressive lattice strain from the substrate, resulting in an in-

plane lattice distortion. **Figure 3-6(b)** shows the AFM results for the flat LBSO sheet. The root mean square of the surface roughness is 0.9 nm, indicating that the surface of the sheet is not coarse.

Next, we discuss the optical properties of the flat LBSO sheets. **Figure 3-7(a)** shows the optical transmission and reflection spectra as functions of wavelength. In the visible light region, at a wavelength range of 380–780 nm, the transmission value was higher than 73%, indicating the visible light transparency of the LBSO sheet. The optical bandgap of the flat LBSO sheet was estimated from the Tauc plot of the $(\alpha h\nu)^2$–$h\nu$ curve, where α denotes the absorption coefficient and $h\nu$ is the photon energy (**Figure 3-7(b)**). The optical bandgap (E_g) of the LBSO sheet was 3.5 eV, which was almost equal to that of bulk LBSO single crystals (3.5 eV) (*1*) and LBSO epitaxial films on MgO substrates (3.55 eV) (*8*).

Figure 3-8 shows the temperature (T) dependence of the electrical conductivity (σ) of the flat LBSO sheet. The σ value increased with decreasing T, indicating that the flat LBSO sheet was a degenerated semiconductor. Similar behavior was also observed in LBSO films on STO and MgO substrates *(8, 19)*. The σ value and Hall mobility (μ) of the flat LBSO sheet at 300 K were 1.9×10^3 S/cm and 80 $cm^2V^{-1}s^{-1}$, respectively. The Hall mobility was slightly lower than that of the LBSO film on the STO substrate (96 $cm^2V^{-1}s^{-1}$) (*20*) because of the lower crystallinity of the sheet (**Figure 4(a)**). According to a previous study, LBSO films grown on mica substrates also exhibit flexibility (*21*). However, σ of the LBSO film on the mica substrate was one order of magnitude lower (σ

= 140 S/cm) than that of the flat LBSO sheet (*21*), indicating significantly lower electron mobility of the LBSO film on the mica substrate. In comparison to other TCOs grown on glass, such as ITO (E_g = 3.6 eV, μ = 54 $cm^2V^{-1}s^{-1}$) (*15*), Al-doped ZnO (E_g = 3.0 eV, μ = 46 $cm^2V^{-1}s^{-1}$) (*16*), and F-doped SnO_2 (E_g = 4.3 eV, μ = 15 $cm^2V^{-1}s^{-1}$) (*14*), the LBSO sheet (E_g = 3.5 eV, μ = 80 $cm^2V^{-1}s^{-1}$) exhibits higher electron mobility. In addition to TCOs, graphene (*12*) and carbon nanotubes (*11*) are also promising candidates for fabricating transparent electrodes. However, they tend to suffer from instability at the edges, restricting their potential applications (*22*). Silver colloids have also garnered considerable attention owing to their high transparency and mobility (*23*), although it is still necessary to improve their particle size consistency and reproducibility (*24*). LBSO has several advantages, including stability against high temperature and humidity, does not use expensive elements such as indium, and high transparency and mobility, which demonstrate its high potential for optoelectronic applications.

3.4. Conclusion

In this study, we successfully obtained large-size rolled and flat crack-free LBSO sheets through a lift-off and transfer method using a water-soluble SAO layer and a-Al_2O_3 protection layer. The rolled sheet had a tubular shape with a height of 5 mm and a diameter of 1 mm, whereas the lateral size of the flat sheet was 5 mm × 5 mm. The significantly large crack-free area was achieved because of the presence of the a-Al_2O_3 protection layer. The difference in curvature between the rolled and flat sheets was as large as 2 mm^{-1}, indicating the excellent flexibility of the LBSO sheets. The LBSO sheet exhibited a wide E_g of 3.5 eV and high Hall mobility of 80 $cm^2V^{-1}s^{-1}$, demonstrating high potential for next-generation optoelectronic device applications.

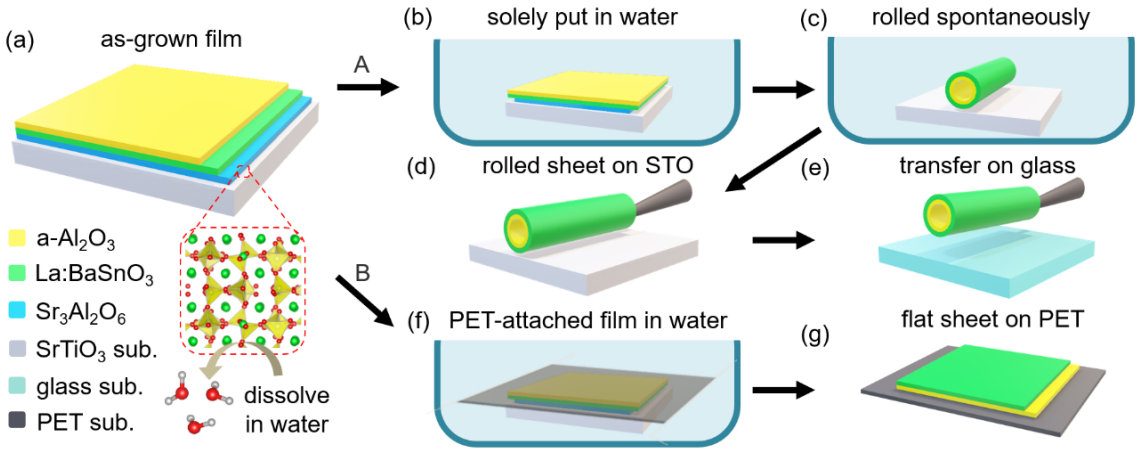

Figure 3-1. Schematics of the synthesis process of the LBSO sheets. (a) As-grown film, (b) the film in pure water, rolled sheet on STO substrate in (c) water and (d) air, € rolled sheet transferred onto glass. (f) PET-attached as-grown film in pure water, and (g) flat sheet on PET.

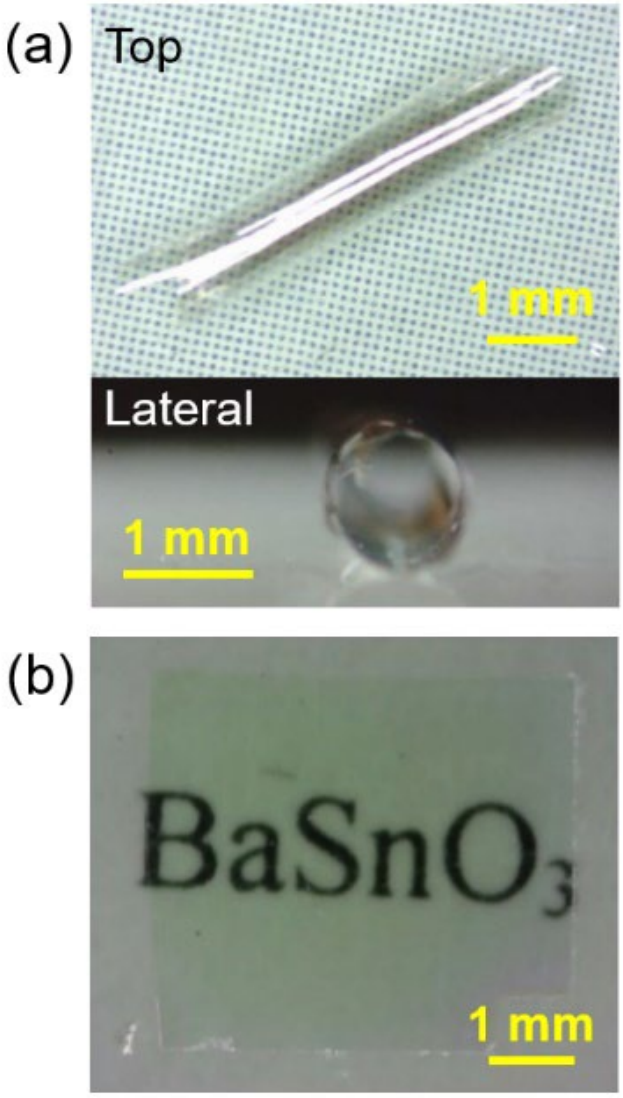

Figure 3-2. Transfer of LBSO sheet on glass and PET substrates. (a) Top and lateral view photographs of the rolled LBSO sheet transferred onto glass and (b) photograph of the flat LBSO sheet on the PET substrate.

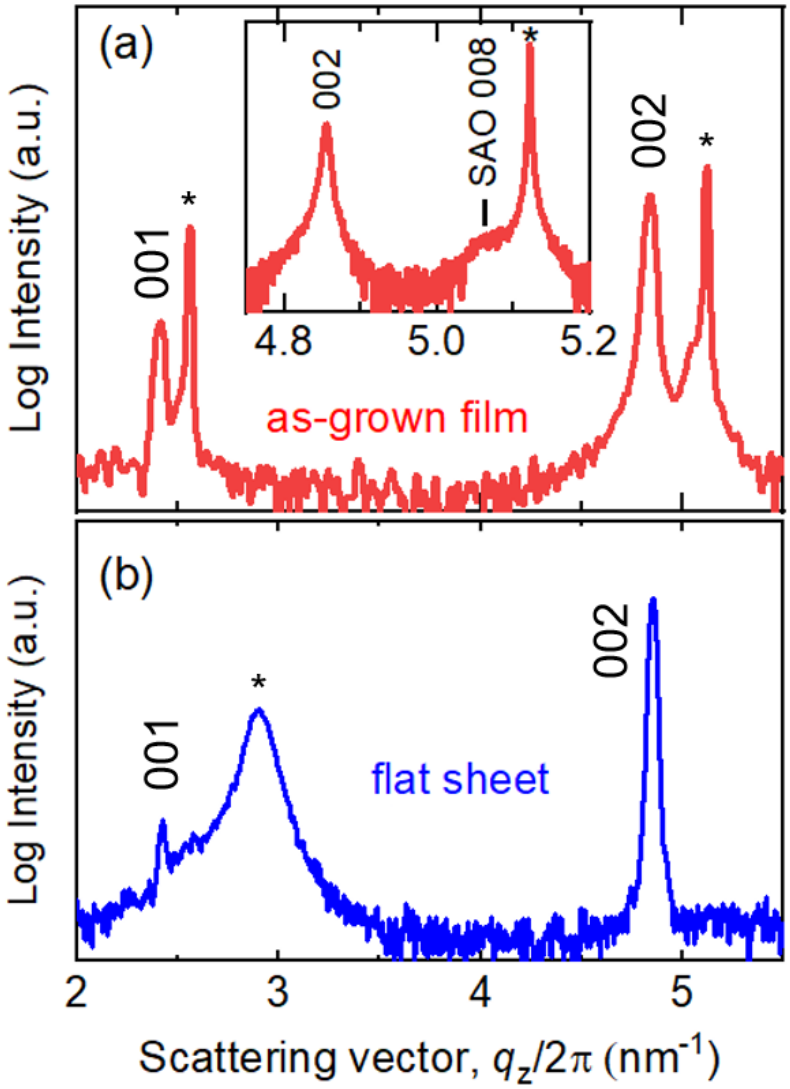

Figure 3-3. Out-of-plane XRD patterns of as-grown film and sheet. Out-of-plane XRD patterns of (a) the as-grown film and (b) flat LBSO sheet on the PET substrate. Asterisks correspond to the STO or PET substrates.

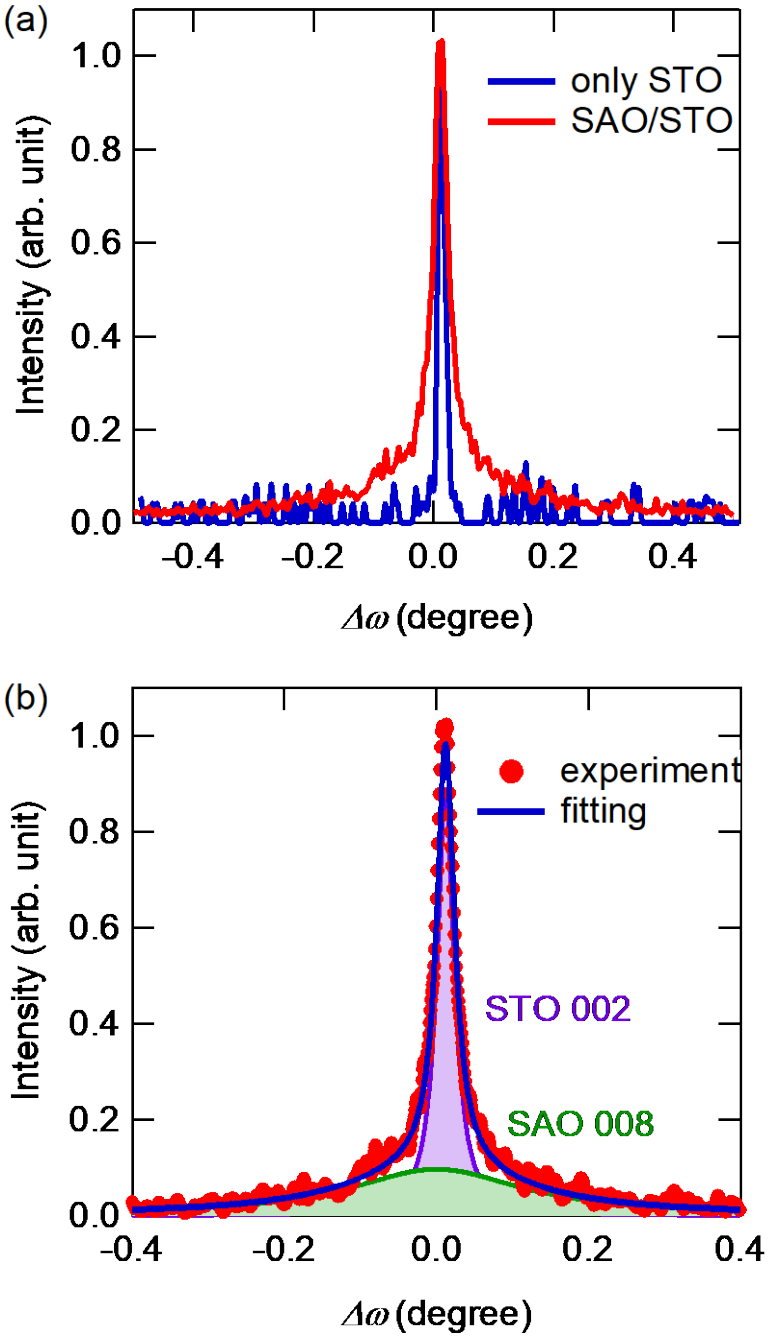

Figure 3-4. Rocking curve of the LBSO sheet. (a) Rocking curves at $q_z/2\pi$ = 5.06 nm^{-1} for the SAO/STO film and only STO substrate. (b) Experiment and fitting results of the rocking curves at $q_z/2\pi$ = 5.06 nm^{-1} for the SAO/STO film.

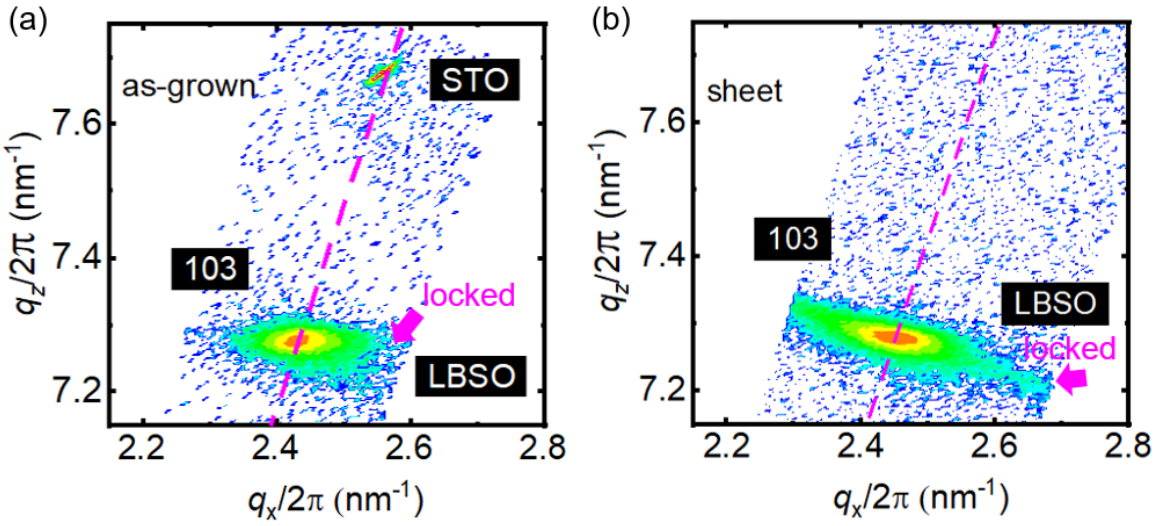

Figure 3-5. Reciprocal space map of as-grown film and sheet. Reciprocal space map of the (c) as-grown film and (b) flat sheet on PET substrate.

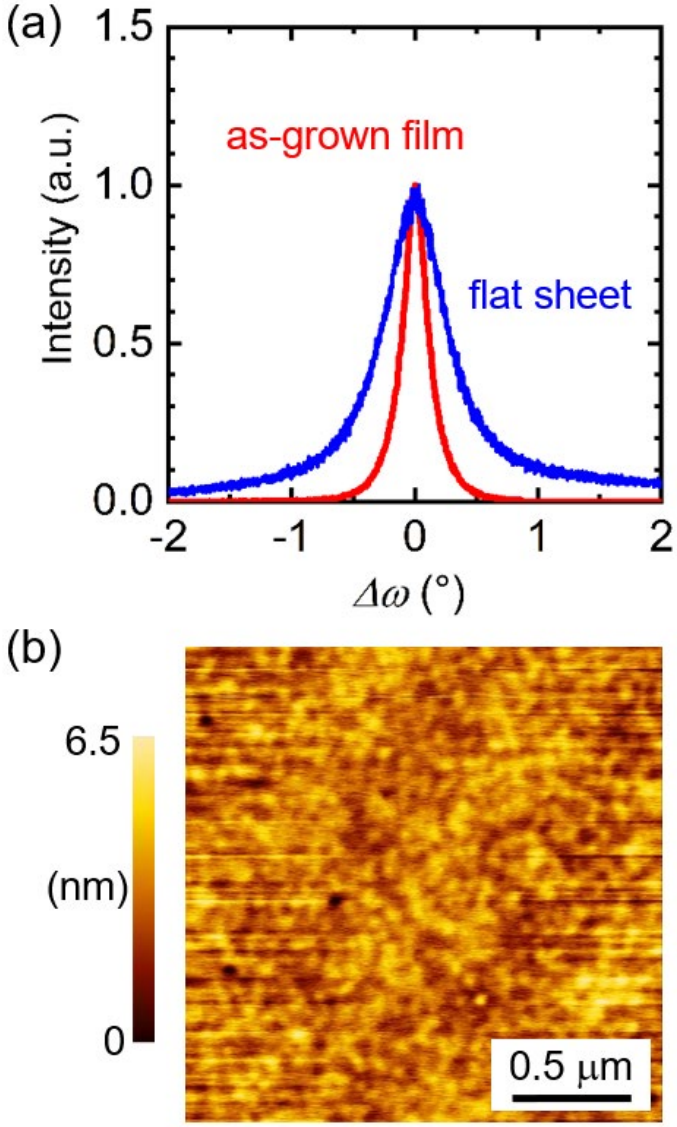

Figure 3-6. Rocking curves and AFM imagine of LBSO sheet. (a) Rocking curves of the 002 diffraction peak of the as-grown film and flat LBSO sheet. (b) AFM image of the flat LBSO sheet.

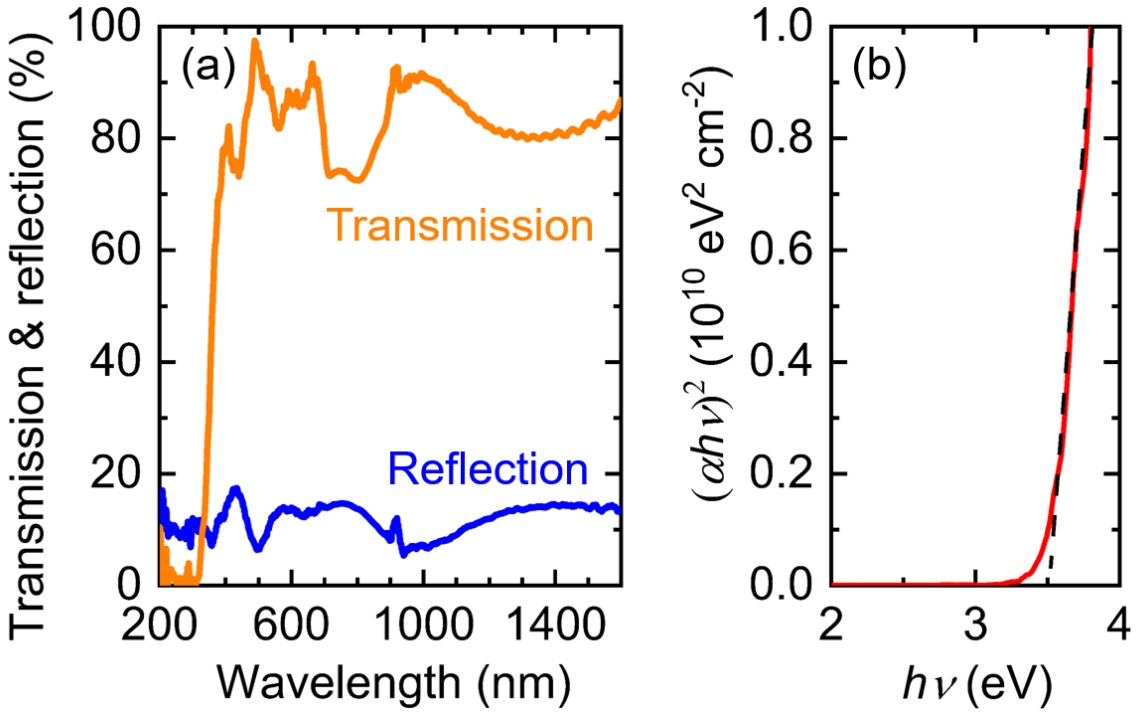

Figure 3-7. Optical property of LBSO sheet. (a) Optical transmission and reflection spectra as functions of wavelength, and (b) photon energy dependence of $(\alpha h\nu)^2$ of the flat LBSO sheet.

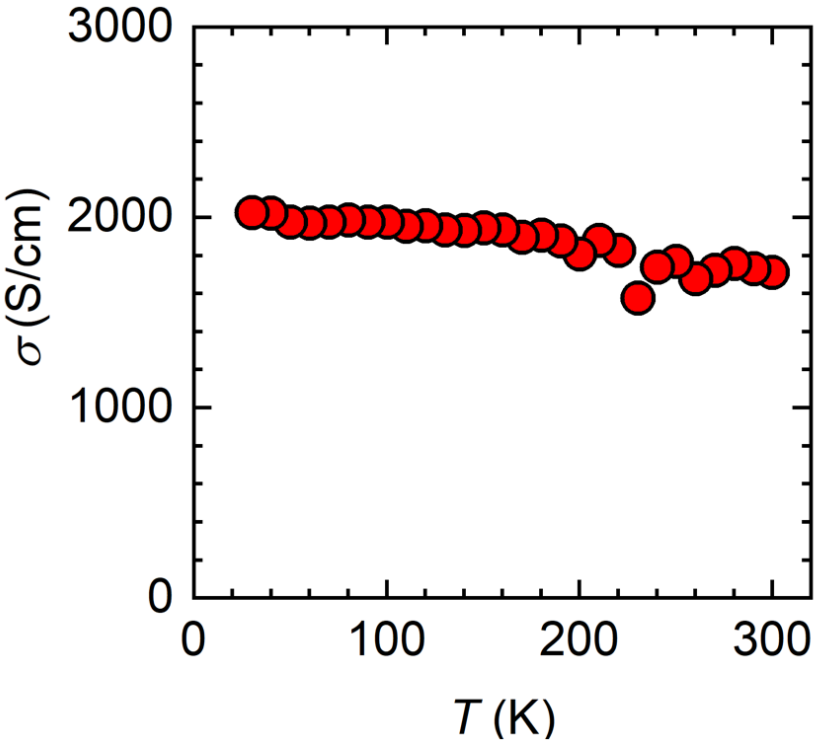

Figure 3-8. Low temperature conductivity of LBSO sheet. Temperature dependence of the electrical conductivity of the flat LBSO sheet.

References

1. H. J. Kim *et al.*, High mobility in a stable transparent perovskite oxide. *Applied Physics Express* **5**, 061102 (2012).

2. S. S. Shin *et al.*, Improved quantum efficiency of highly efficient perovskite $BaSnO_3$-based dye-sensitized solar cells. *ACS nano* **7**, 1027−1035 (2013).

3. F. Xie, Y. Li, T. Xiao, D. Shen, M. Wei, Efficiency improvement of dye-sensitized BaSnO3 solar cell-based surface treatments. *Electrochim. Acta* **261**, 23−28 (2018).

4. S. S. Shin *et al.*, Colloidally prepared La-doped $BaSnO_3$ electrodes for efficient, photostable perovskite solar cells. *Science* **356**, 167−171 (2017).

5. H. J. Kim *et al.*, Physical properties of transparent perovskite oxides (Ba, La) SnO_3 with high electrical mobility at room temperature. *Phys. Rev. B.* **86**, 165205 (2012).

6. Y. M. Kim, C. Park, U. Kim, C. Ju, K. Char, High-mobility $BaSnO_3$ thin-film transistor with HfO_2 gate insulator. *Appl. Phys. Express.* **9**, 011201 (2015).

7. H. Paik *et al.*, Adsorption-controlled growth of La-doped $BaSnO_3$ by molecular-beam epitaxy. *APL Mater.* **5**, 116107 (2017).

8. A. V. Sanchela *et al.*, Large thickness dependence of the carrier mobility in a transparent oxide semiconductor, La-doped $BaSnO_3$. *Appl. Phys. Lett.* **112**, 232102 (2018).

9. J. Bernède, L. Cattin, M. Morsli, Y. Berredjem, Ultra-thin metal layer passivation of the transparent conductive anode in organic solar cells. *Sol. Energy Mater. Sol. Cells* **92**, 1508−1515 (2008).

10. J. Kwak *et al.*, Near room-temperature synthesis of transfer-free graphene films. *Nat. Commun.* **3**, 645 (2012).

11. L.-M. Peng, Z. Zhang, S. Wang, Carbon nanotube electronics: recent advances. *Mater. Today* **17**, 433−442 (2014).

12. X. Huang, Z. Zeng, Z. Fan, J. Liu, H. Zhang, Graphene‐based electrodes. *Adv. Mater.* **24**, 5979−6004 (2012).

13. D. Kumar, R. Sharma, Advances in conductive polymers. *Eur. Polym. J.* **34**, 1053–1060 (1998).

14. H. Kim, R. Auyeung, A. Piqué, Transparent conducting F-doped SnO_2 thin films grown by pulsed laser deposition. *Thin Solid Films* **516**, 5052–5056 (2008).

15. O. Tuna, Y. Selamet, G. Aygun, L. Ozyuzer, High quality ITO thin films grown by dc and RF sputtering without oxygen. *J. Phys. D: Appl. Phys.* **43**, 055402 (2010).

16. S. Cornelius *et al.*, Achieving high free electron mobility in ZnO: Al thin films grown by reactive pulsed magnetron sputtering. *Appl. Phys. Lett.* **94**, 042103 (2009).

17. P. Singh *et al.*, Large-Area Crystalline $BaSnO_3$ Membranes with High Electron Mobilities. *ACS Applied Electronic Materials* **1**, 1269–1274 (2019).

18. G. A. Rosales-Sosa, A. Masuno, Y. Higo, H. Inoue, Crack-resistant Al_2O_3–SiO_2 glasses. *Sci. Rep.* **6**, 1–7 (2016).

19. A. V. Sanchela, T. Onozato, B. Feng, Y. Ikuhara, H. Ohta, Thermopower modulation clarification of the intrinsic effective mass in transparent oxide semiconductor $BaSnO_3$. *Phys. Rev. Mater.* **1**, 034603 (2017).

20. A. V. Sanchela *et al.*, Buffer layer-less fabrication of a high-mobility transparent oxide semiconductor, La-doped $BaSnO_3$. *J. Mater. Chem. C* **7**, 5797–5802 (2019).

21. W. Sun *et al.*, High optical transmittance and anomalous electronic transport in flexible transparent conducting oxides $Ba_{0.96}La_{0.04}SnO_3$ thin films. *Ceram. Int.* **44**, 18001–18006 (2018).

22. Ç. O. Girit *et al.*, Graphene at the edge: stability and dynamics. *Science* **323**, 1705–1708 (2009).

23. M. Wu, S. Yu, L. He, L. Yang, W. Zhang, High quality transparent conductive Ag-based barium stannate multilayer flexible thin films. *Sci. Rep.* **7**, 103 (2017).

24. I. Pastoriza-Santos, L. M. Liz-Marzán, Colloidal silver nanoplates. State of the art and future challenges. *J. Mater. Chem.* **18**, 1724–1737 (2008).

Chapter 4. Bulk-like Ferroelectricity, Permittivity, and Enhanced Tunability in Millimeter-size Crack-free $Ba_{1-x}Sr_xTiO_3$ Flexible Epitaxial Sheets

4.1. Purpose of this chapter

The history $Ba_{1-x}Sr_xTiO_3$ (BST) is originated from most famous perovskite ferroelectric material $BaTiO_3$ (BTO), which was discovered during World War II in 1941 and 1944 in the United States, Russia, and Japan. After nearly 80 years of development, BTO and its derivative materials have become fundamental components in modern electronic devices, such as capacitors (*1*), satellite antennas (*2*), filters (*3*), and more. The crystal structure of BST is a typical perovskite structure, and changing from tetragonal to cubic when increasing x value duo to the different bond lengths in the barium-oxygen and strontium--oxygen bonds. Therefore, in BST compositions, for example, when x= 0.25, BST exhibits ferroelectric properties, and the crystal structure is a tetragonal perovskite structure similar to BTO. Conversely, when x= 0.5, BST exhibits paraelectric properties, and the crystal structure is a cubic perovskite structure similar to STO.

The development of flexible ferroelectric materials is crucial for the advancement of various emerging technologies, including microelectromechanical systems (*4*), vibrational energy harvesters (*5, 6*), and wearable electronics (*7*). Among the utilized ferroelectric materials, perovskite BTO and BST stand out owing to their desirable

properties such as dielectric permittivity (ε_r), tunability of ε_r, piezoelectricity, non-toxicity, and stability. These materials have been widely used in electronic components such as multilayer ceramic capacitors and microwave devices (*8, 9*). However, perovskite oxides, including BST, are inherently rigid, necessitating thickness reduction to sub-micrometer levels to achieve flexibility. Moreover, in the case of flexible ferroelectric sheets, controlling the crystal orientation is crucial for achieving high electrical performance.

In this chapter, I successfully obtained crack-free millimeter-sized epitaxial sheets of BST with composition ratios of x = 0.25 and 0.5. This was accomplished using lift-off and transfer techniques combined with the use of an a-Al_2O_3 protection layer with a thickness greater than 10 nm. Various bottom electrode materials were prepared, including a- and polycrystalline (poly-) indium tin oxide (ITO), poly-RuO_2, and $SrRuO_3$. Among these options, poly-ITO was found to be the most suitable electrode material. The BST sheet with a composition of x = 0.25 demonstrated outstanding ferroelectric properties similar to bulk single crystals, while the BST sheet with a composition of x = 0.5 simultaneously exhibited high permittivity (ε_r ~3500 at 10 kHz) and high tunability (56%). This was attributed to the release of the substrate-induced strain in the free-standing sheet.

4.2. Experimental

Synthesis of freestanding $Ba_{1-x}Sr_xTiO_3$ sheet: As-grown $Ba_{1-x}Sr_xTiO_3$ (x = 0.25 and 0.5) epitaxial films were fabricated on SAO-buffered $SrTiO_3$ (001) (STO) substrates using the pulsed laser deposition (PLD) method. Typical thicknesses of the SAO and BST layers were 20 and 300 nm, respectively. The film deposition process involved maintaining the substrate temperature (T_s) and oxygen pressure (P_{O2}) at 850 °C and 1×10^{-3} Pa for the SAO layer and at 850 °C and 0.5 Pa for the BST layer, respectively. The electrode and a-Al_2O_3 protective layers were deposited on top of the BST layer using the PLD method. Four types of oxide electrode materials were used as the electrode layers: a-ITO, poly-ITO, epitaxial $SrRuO_3$, and poly-RuO_2. The T_s and P_{O2} values were 25 °C and 5 Pa for a-ITO, 200 °C and 5 Pa for poly-ITO, 600 °C and 30 Pa for epitaxial $SrRuO_3$, and 200 °C and 10 Pa for poly-RuO_2, respectively. Meanwhile, the a-Al_2O_3 layer was deposited at a T_s of 25 °C and P_{O2} of 1×10^{-3} Pa. The typical thicknesses of the electrode and a-Al_2O_3 layers were 100 and 10–1000 nm, respectively. To peel off the a-Al_2O_3/electrode/BST tri-layer from the STO substrate, the as-grown film was placed in pure water for 24 h to completely dissolve the SAO layers. Before the as-grown film was placed in pure water, its surface was attached to an adhesive-coated PET substrate (Kimoto Co., Ltd., Prosave™ UV).

***Crystallographic analyses*:** The crystal structures of the as-grown films and obtained sheets were determined using X-ray diffraction (XRD) measurements (Cu $K\alpha_1$, ATX-G,

Rigaku Co.).

***Ferroelectricity & dielectric property measurements*:** To measure the dielectric and ferroelectric properties of the sheets, 100-μm-diameter Pt electrodes were deposited on top of the sheet, that is, the BST layer, as the top electrodes. Dielectric properties were evaluated using an LCR meter (E4980A; Keysight Technologies, Inc.). The ferroelectric properties of the sheets were measured using a ferroelectric tester (Multiferroic II, Radiant Technologies, Inc.).

4.3. Result and discussion

The as-grown films on the $SrTiO_3$ substrates consisted of four layers: a-Al_2O_3, electrode, $Ba_{1-x}Sr_xTiO_3$ (BST), and $Sr_3Al_2O_6$ (SAO), as illustrated in **Figure 4-1(a)**. Before placing the as-grown film in pure water, an adhesive-layer-coated PET substrate was attached to the surface. Thereafter, the as-grown PET-attached films were placed in pure water for 24 h. The sheet could be peeled off from the STO substrate because the SAO sacrificial layer completely dissolved in water. **Figure 4-1(b)** shows a photograph of the sheet obtained on the PET substrate. The sheet consists of BST with a composition of $x = 0.5$, poly-ITO, and 1-μm-thick a-Al_2O_3 tri-layer, where the top surface of the sheet was the BST layer. The lateral size of the sheet was 5 mm × 5 mm, and no significant cracks were observed. In addition, the sheets were flexible.

Figures 4-1(c, d) show the out-of-plane XRD patterns of the as-grown films with compositions of $x = 0.25$ and 0.5. In both films, the 001 and 002 diffraction peaks of BST were clearly observed. Because poly-ITO was used as the electrode layer, the 222 diffraction peaks of ITO also appeared at $q_z/2\pi = 3.4$ nm^{-1}. The in-plane orientation was evaluated using reciprocal space mapping (RSM) measurements of approximately 103 diffraction peaks (**Figure 4-2**). Spot-like 103 peaks were observed in the two as-grown films, confirming the epitaxial growth of BST layers on the SAO layer. The epitaxial growth of the BST layers is derived from the fact that the arrangement of Sr ions in the SAO layer is similar to that of the Ba/Sr ions in the BST layers. In addition, *a*-axis lengths

of bulk BST are also similar to $a/4$ of bulk SAO, 3.961 Å (*10*); bulk BST with $x = 0.25$ has a tetragonal structure with $a = 3.980$ and $c = 3.992$ Å, whereas bulk BST with $x = 0.5$ has a cubic structure with $a = 3.957$ Å (*11, 12*). The lattice constants of the as-grown BST films were evaluated from the out-of-plane XRD and RSM results. For the $x = 0.25$ film, the out-of-plane lattice constant (3.991 Å) was greater than that of the in-plane one (3.97 Å), indicating that the BST layer was *c*-axis oriented. In contrast, the in-plane and out-of-plane lattice constants were similar for the $x = 0.5$ film: 3.95 and 3.957 Å, respectively.

The as-grown BST films were peeled off from the STO substrates and transferred onto PET substrates. The diffraction peaks of STO disappeared, whereas those of PET appeared in the out-of-plane XRD patterns (**Figure 4-1(c, d)**). The BST sheets exhibited 001 and 002 diffraction peaks, indicating that the crystal orientation was maintained even after the BST sheets were peeled off from the substrate. The lattice constants of the sheets were evaluated from their out-of-plane and in-plane XRD patterns (**Figure 4-1(c, d)**, and **Figure 4-3**). The out-of-plane lattice constant of the $x = 0.25$ film (3.984 Å) was greater than that of the in-plane one (3.97 Å), indicating that the *c*-axis orientation was maintained during the sheet synthesis process. This growth orientation is preferred for the ferroelectric measurements because bulk BST with a composition of $x = 0.25$ exhibits spontaneous polarization along the *c*-axis. Meanwhile, for the $x = 0.5$ film, the in-plane and out-of-plane lattice constants were almost equal (3.95 and 3.950 Å, respectively), indicating that it has an almost cubic structure, which agrees with the bulk BST with a composition of $x = 0.5$.

Figure 4-4 shows photographs of the x = 0.5 sheets as a function of the thickness of the a-AlO_x protective layer. When a protective layer was not used, a high density of cracks was generated in the sheet. However, the use of a 10-nm-thick a-AlO_x layer significantly suppressed crack generation, resulting in a maximum crack-free area of 1.5 mm^2. The size of the crack-free area increased with the thickness of the a-AlO_x layer. When the thickness of the a-AlO_x layer was 1 μm, no cracks appeared on the BST sheets.

Figure 4-5(a) shows the SEM image of the BST sheet. Cracks were not observed, but a light-colored line extending diagonally downward from the upper left of the figure was observed. The enlarged view of the SEM image is shown in **Figure 4-5 (b)**, where the right and left sides are the lighter- and darker-colored areas in **Figure 4-5 (a)**, respectively. In the lighter-colored area, wrinkles with a width of ~10 μm appeared at intervals of a few μm. Additionally, in all the areas, fine wrinkles spread in a mosaic pattern. Many wrinkles were not observed in the SEM image of the LSSO sheet (**Figure 4-1(f)**). In contrast to LSSO, perovskite ferroelectric oxides consist of many domains and boundaries. For example, even in the *c*-axis-oriented films, the *a*-domain is formed between upward and downward polarized *c*-domains as illustrated in **Figure 4-5 (c)** (*13*). The domain boundary between *a*- and *c*-domains receives a large strain owing to the formation of largely bent lattices (orange lattices in **Figure 4-5 (c)**). Thus, when restraint from the substrate is removed without a capping layer, a force is applied to the sheet to relax the largely bent lattices, resulting in the generation of cracks (**Figure 4-5 (d)**). By contrast, by using a capping oxide layer, the layer hinders the generation of cracks because of the

high crack resistance and/or high Young's modulus of the Al_2O_3 glass (*14, 15*). However, to slightly relax the largely bent lattices, wrinkles are generated instead of cracks in the sheet (**Figure 4-5 (e)**).

To evaluate the ferroelectric and dielectric properties of the BST sheets, preparation of electrode layers between the BST and a-Al_2O_3 layers is necessary. Four representative oxide electrode materials: a-ITO, poly-ITO, epitaxial $SrRuO_3$, and poly-RuO_2 layers, were used as the electrode layers. **Figure 4-6** shows photographs of the x = 0.5 sheets using these electrode layers. The thicknesses of the electrode and a-Al_2O_3 layers were 100 and 1 μm, respectively. When the poly-ITO and RuO_2 layers were used, no cracks were observed in the sheets with lateral sizes of 5 mm × 6 mm and 5 mm × 5 mm, respectively. Several scratches were observed on the sheet containing the a-ITO layer. In contrast, when the epitaxial $SrRuO_3$ layer was used, several wrinkles appeared on the sheet. This is attributed to the higher deposition temperature of the $SrRuO_3$ layer (600 °C) compared to the other electrode layers (25–200 °C). The difference in the thermal expansion coefficients of the BST and $SrRuO_3$ layers causes a greater strain when the film is cooled from the growth temperature to room temperature, which provides a driving force for the generation of wrinkles. These results indicate that a material with a low deposition temperature is suitable as an electrode layer.

Figure 4-7 shows frequency dependence of permittivity (ε_r) and dielectric loss (tan δ) values for the BST sheets at 25 °C as a function of the type of the electrode layers. A Pt electrode was used as the top electrode. In both the x = 0.25 and 0.5 sheets, the highest ε_r

values were observed when using the poly-ITO electrodes. This is probably due to the higher electrical conductivity of the poly-ITO layer compared to that of the a-ITO and poly-RuO_2 layers. The electrical conductivities of the poly-ITO, a-ITO, and poly-RuO_2 films deposited on the glass were 3×10^3, 2×10^2, and 2×10^3 S/cm, respectively. In addition, it has been reported that RuO_2 films grown at low temperatures, such as those used in this study, tend to have a higher concentration of oxygen vacancies (*16*), probably resulting in a decrease in ε_r of BST at the BST/RuO_2 interface. Based on the obtained results, we concluded that poly-ITO is suitable as the bottom electrode for BST epitaxial sheets.

The ε_r values were 1500 and 4000 at 1 kHz for the $x = 0.25$ and 0.5 sheets, respectively, when the poly-ITO electrode was used. The ε_r values of the bulk material are more than twice as large as those of epitaxial films, with values of 700 and 1400, respectively (*17, 18*). Epitaxial thin films grown on substrates are known to typically exhibit a decrease in ε_r compared to their bulk counterparts, owing to the strain induced by the substrate (*11, 19*). However, because the BST sheet was peeled off from the substrate, the substrate-induced strain was not observed in the sheet. This strain relaxation from the substrate is probably a contributing factor to the high ε_r of the BST sheet.

Figure 4-7(e, f) shows the ε_r and tan δ values of the $x = 0.25$ sheet as a function of bending times. In this measurement, the sheet was bent with a curvature of 35 mm in an upward direction, and then, the sheet was returned to a flat state for measurement. Even after such bending was repeated and returned 4000 times, the dielectric properties of the

sheet did not change significantly.

Figure 4-8(a) shows the polarization versus electric field ($P-E$) curve for x = 0.25 sheets. The measurement was conducted at a temperature of 25 °C and frequency of 10 kHz using poly-ITO layer as a bottom electrode. A clear ferroelectric hysteresis loop was observed, along with P reversal current peaks, proving the room-temperature ferroelectricity of the sheet. The remaining P (P_r) and coercive field (E_c) values were 11 μC/cm^2 and 100 kV/cm, respectively. With an increase in the applied maximum E, P_r increased and reached 17 μC/cm^2 (**Figure 4-9**), which was almost equal to that of bulk x = 0.25 single crystal (18 μC/cm^2) (*20*). **Figure 4-8(b)** shows ε_r and tan δ for the x = 0.25 sheet as a function of E at 25 °C. In the ε_r-E curve, a butterfly curve was observed owing to the ferroelectric nature of the x = 0.25 sheet. The tunability ($1-\varepsilon(E)/\varepsilon(E=0)$) of the sheet was 63%, while the tan δ value remained below 0.05.

Figure 4-10(a) shows $P-E$ curve for the x = 0.5 sheet at 25 °C. The tiny hysteresis loop indicates that the x = 0.5 sheet is paraelectric rather than ferroelectric at 25 °C. This is reasonable because Curie temperatures of bulk BST with x = 0.25 and 0.5 were 52 and −30 °C, respectively (*21*). The x = 0.5 sheet also exhibited tunability in the ε_r-E curve (**Figure 4-10(b)**), with a tunability value of 56%.

In bulk BST, the tunability values were approximately 19.6 and 23.7% at x = 0.5 and 0.6, respectively, while the ε_r values ranged from 2500 to 11000 at a composition range of x = 0.5–0.6 (*22, 23*). To further improve the tunability, doping techniques were employed. For instance, MgO-doped bulk BST with a composition of x = 0.6 exhibited a

high tunability of 50% (*24, 25*), while the ε_r value decreased to 2000. In contrast, in thin films, the tunability values were significantly higher, reaching 83% at $x = 0.5$, while the ε_r value was significantly smaller (1800) (*26*). This enhanced tunability in thin films was attributed to the higher breakdown electric field compared to the bulk material owing to the epitaxial structure with reduced grain boundaries and thinner thickness. Meanwhile, the reduced ε_r was derived from the strain induced by the substrate (*27*). In this study, the $x = 0.5$ BST sheet exhibited a high tunability of 56%, similar to what was observed in thin films. In addition, in the BST sheet, the absence of strain from the substrate allowed for a crystalline structure similar to that of the bulk, enabling the maintenance of high ε_r (4000 at 1 kHz).

4.4. Conclusion

In this study, crack-free millimetre-sized BST epitaxial sheets were successfully obtained using lift-off and transfer techniques employing an a- a-Al_2O_3 protective layer with a thickness greater than 10 nm. Poly-ITO is suitable as the bottom electrode of the sheets owing to its high electrical conductivity and low deposition temperature. The x = 0.25 sheet exhibited excellent ferroelectric property, whereas the x = 0.5 sheet simultaneously exhibited high permittivity and tunability owing to the release of substrate-induced strain. These findings indicate that the proposed sheet fabrication process is suitable for obtaining high-quality, highly oriented, flexible ferroelectric, and high-permittivity oxide sheets.

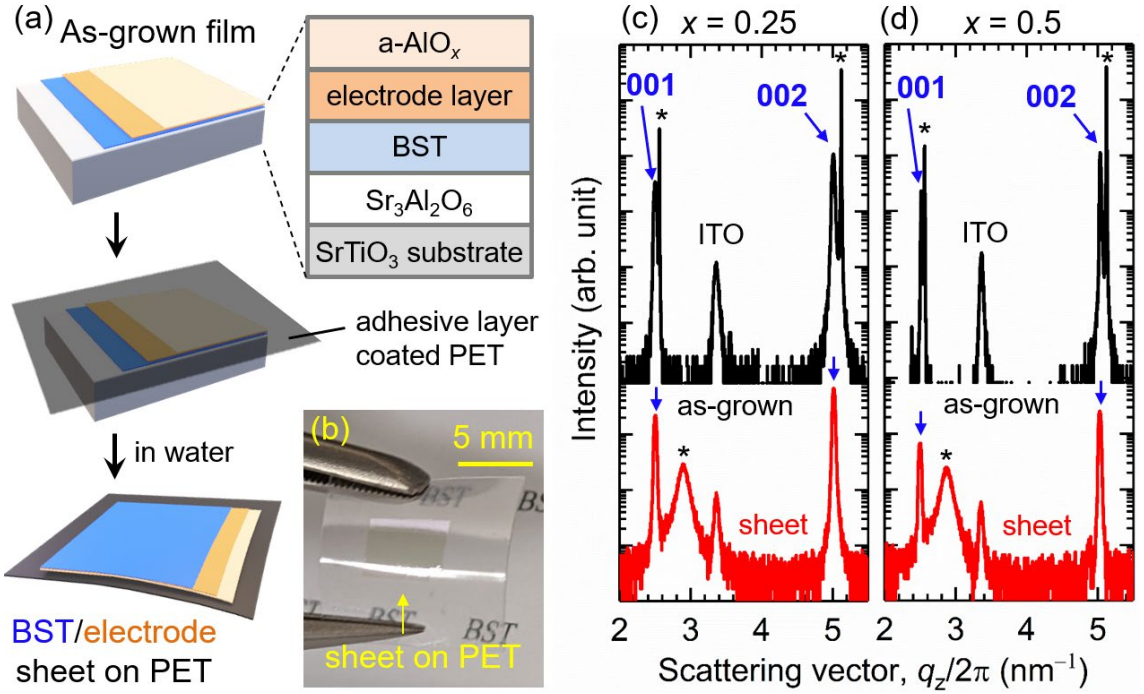

Figure 4-1. Synthesis and characterization of BST sheet. (a) Schematic of the synthesis process of the BST sheet. (b) Photograph of the $x = 0.5$ flexible sheet on the PET substrate. Out-of-plane XRD patterns of the as-grown films and sheets for (c) $x = 0.25$ and (d) $x = 0.5$ with poly-ITO electrodes. The asterisk marks correspond to the STO or PET substrates.

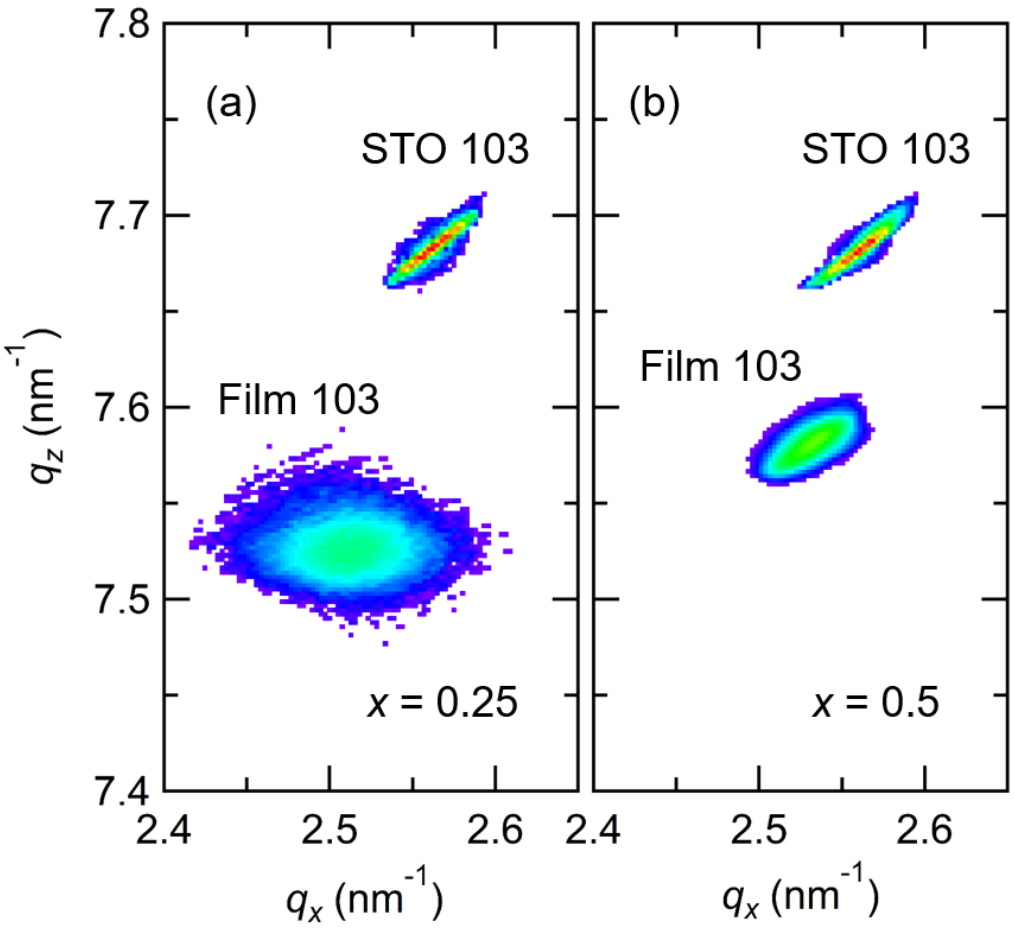

Figure 4-2. RSM of as-grown film (x = 0.25, and 0.5). Reciprocal space maps for the as-grown BST films with x = (a) 0.25 and (b) 0.5.

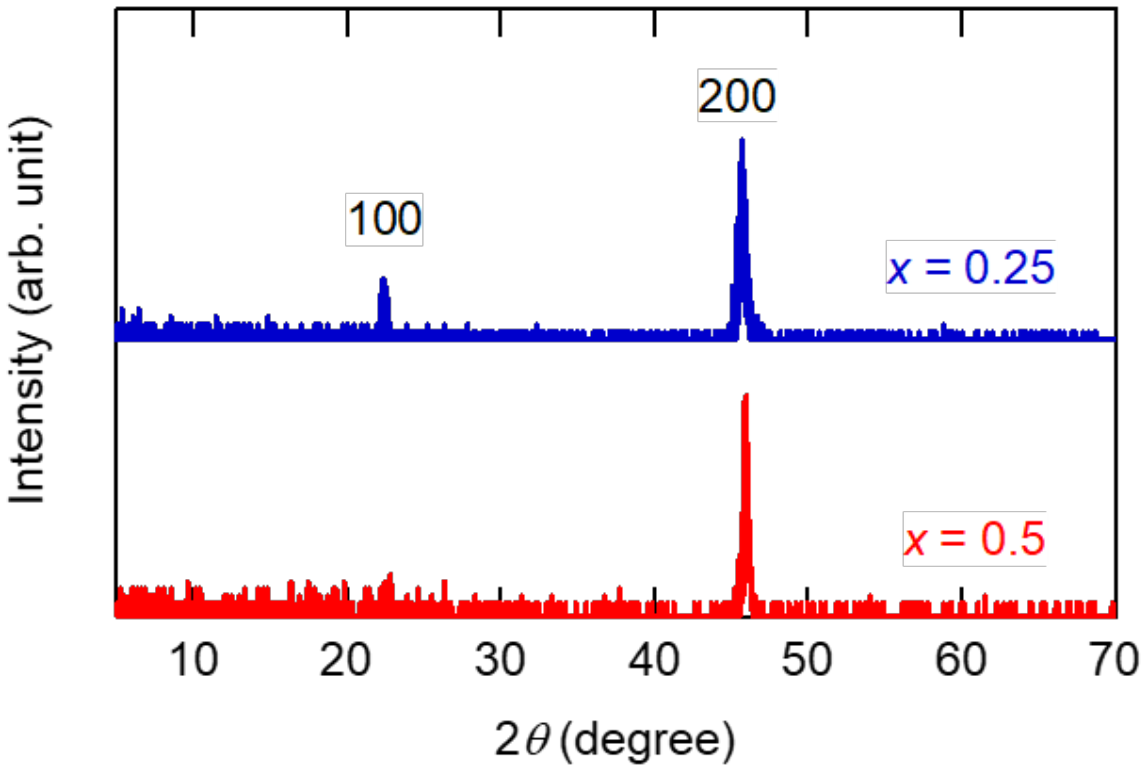

Figure 4-3. In-plane XRD patterns for the x = 0.25 and 0.5 sheets.

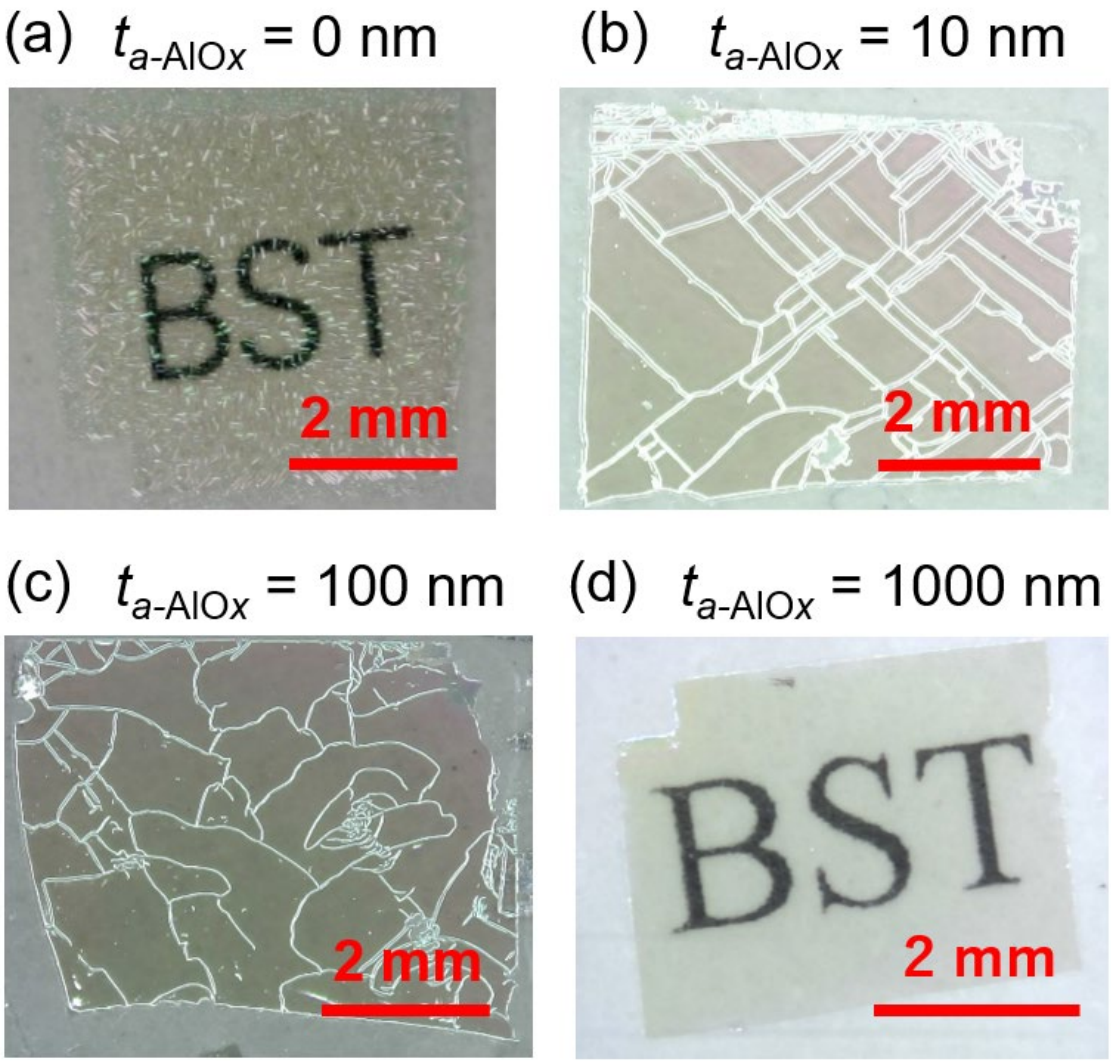

Figure 4-4. Photograph of a-AlO_x protection layer thickness dependence of crack. Photograph of the x = 0.5 sheets with ITO electrodes and a-AlO_x protection layers as a function of thickness of the a-AlO_x layer ($t_{a\text{-}AlOx}$). $t_{a\text{-}AlOx}$ is (a) 0, (b) 10 nm, (c) 100 nm, and (d) 1 μm.

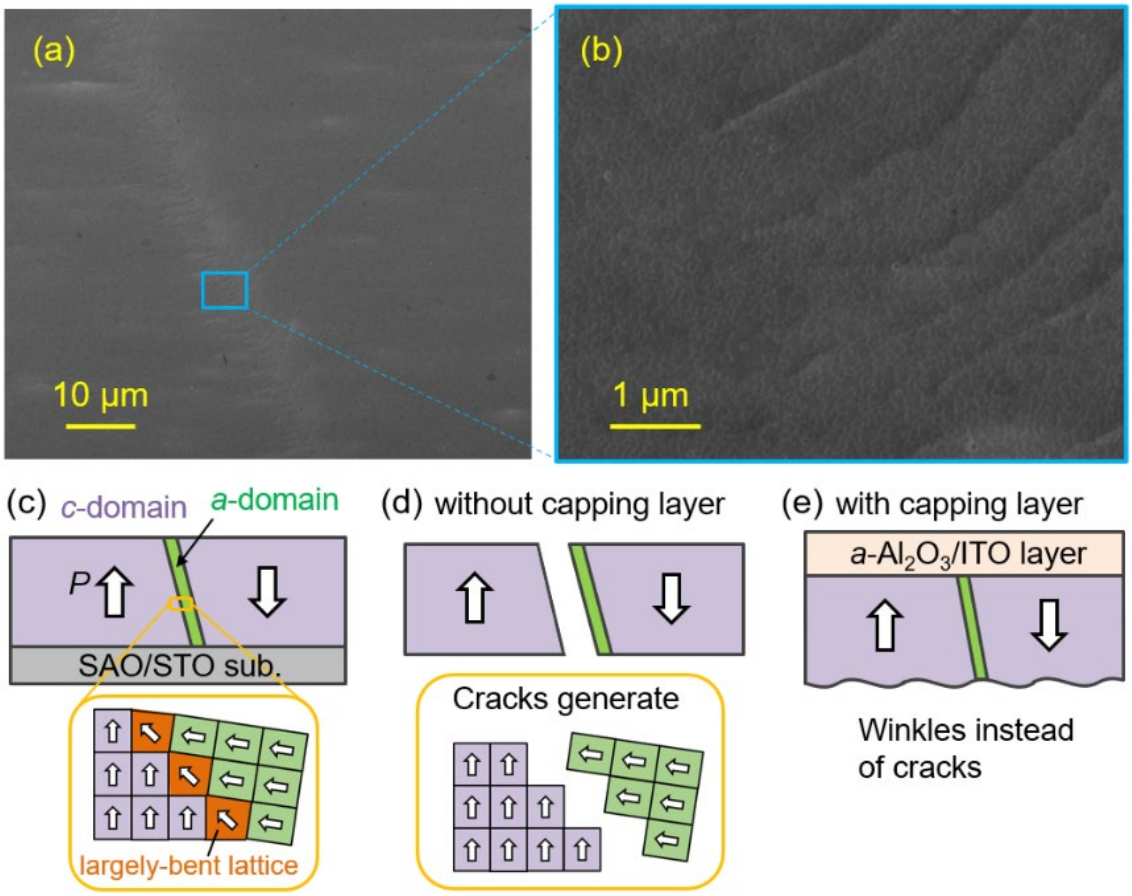

Figure 4-5. Release of lattice distortion in BST sheet. (a) SEM images of the BST sheets with the capping oxide layer. Schematic cross-sectional images of the (c) BST film and BST sheets (d) without and (e) with the capping oxide layer.

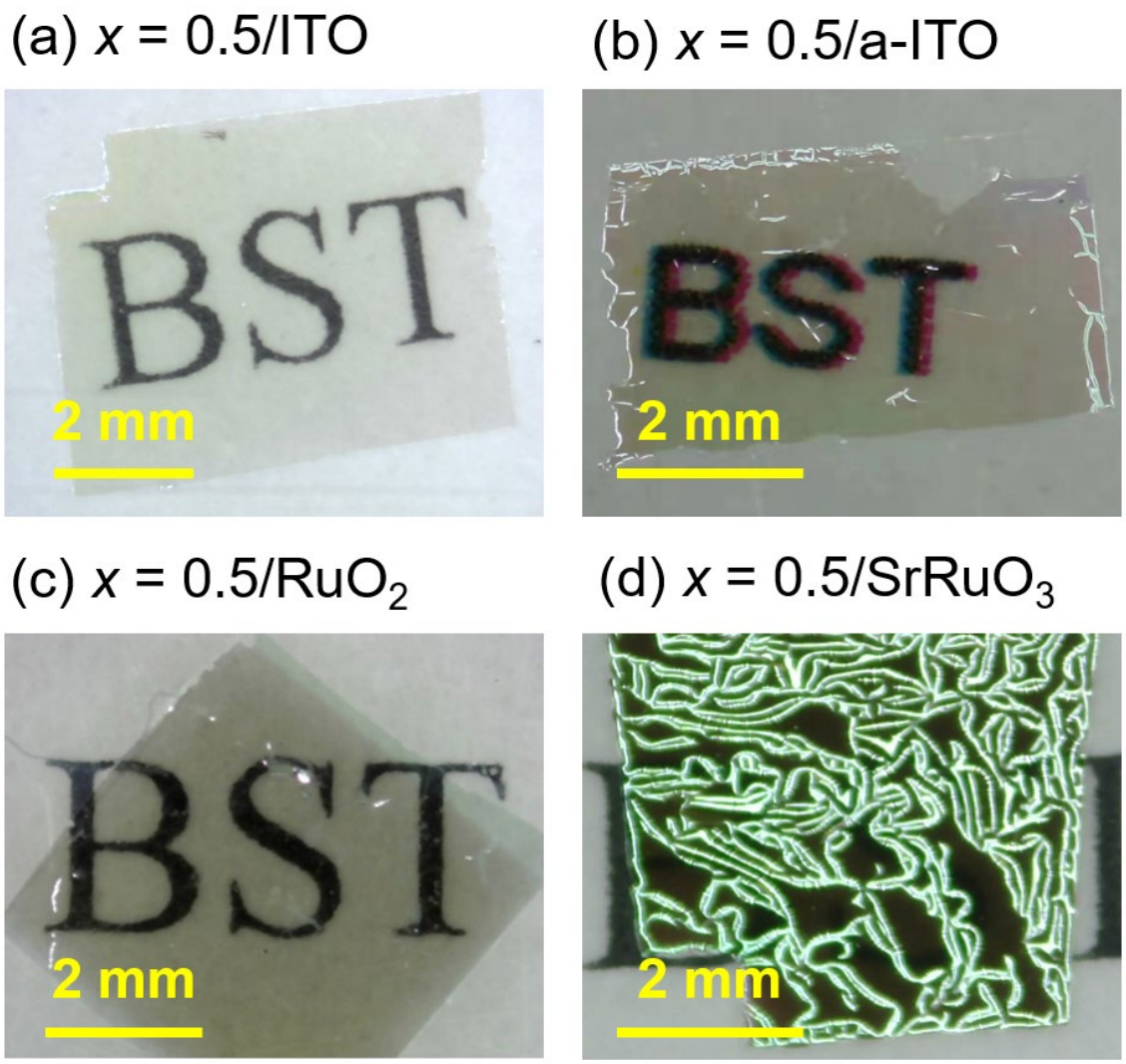

Figure 4-6. Photograph of other protection layers dependence of crack. Photograph of the x = 0.5 sheets using (a) a-ITO, (b) poly-ITO, (c) poly-RuO_2, and (d) epitaxial $SrRuO_3$ as the electrode layers.

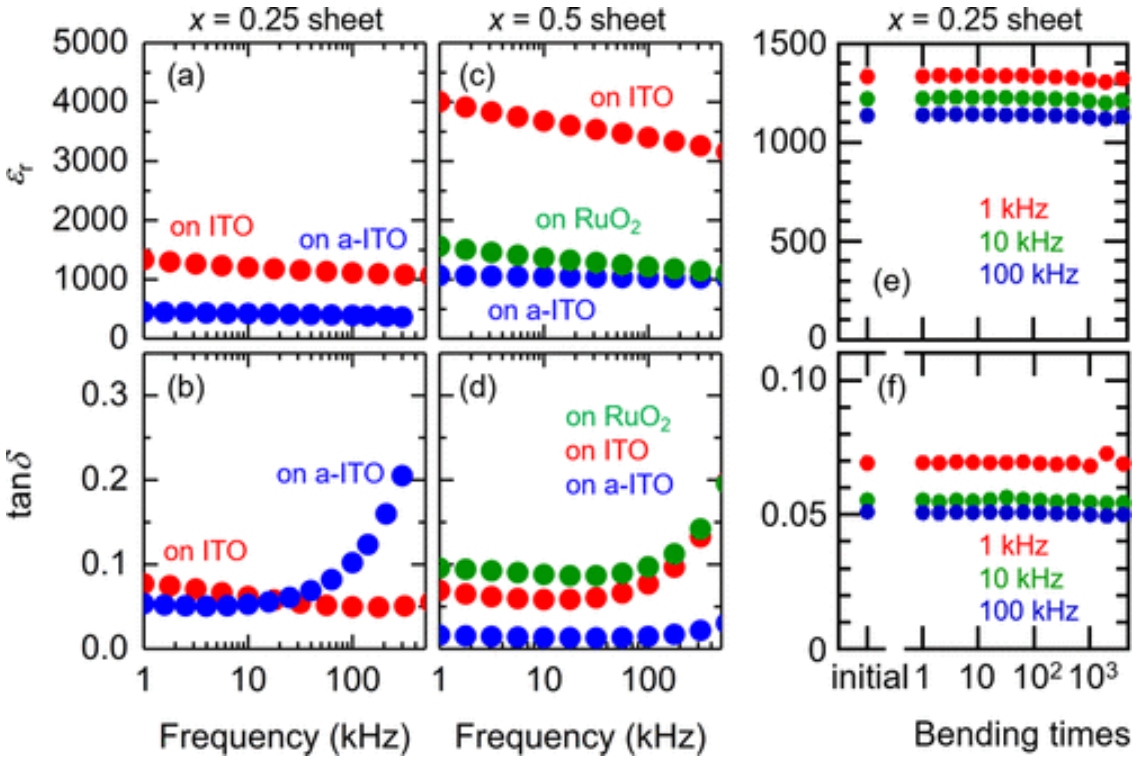

Figure 4-7. Dielectric property and electrode dependence of flexible BST sheet. Frequency dependence of (a) ε_r and (b) tan δ for the x = 0.25 and (c, d) x = 0.5 sheets as a function of electrode layers at 25 °C.

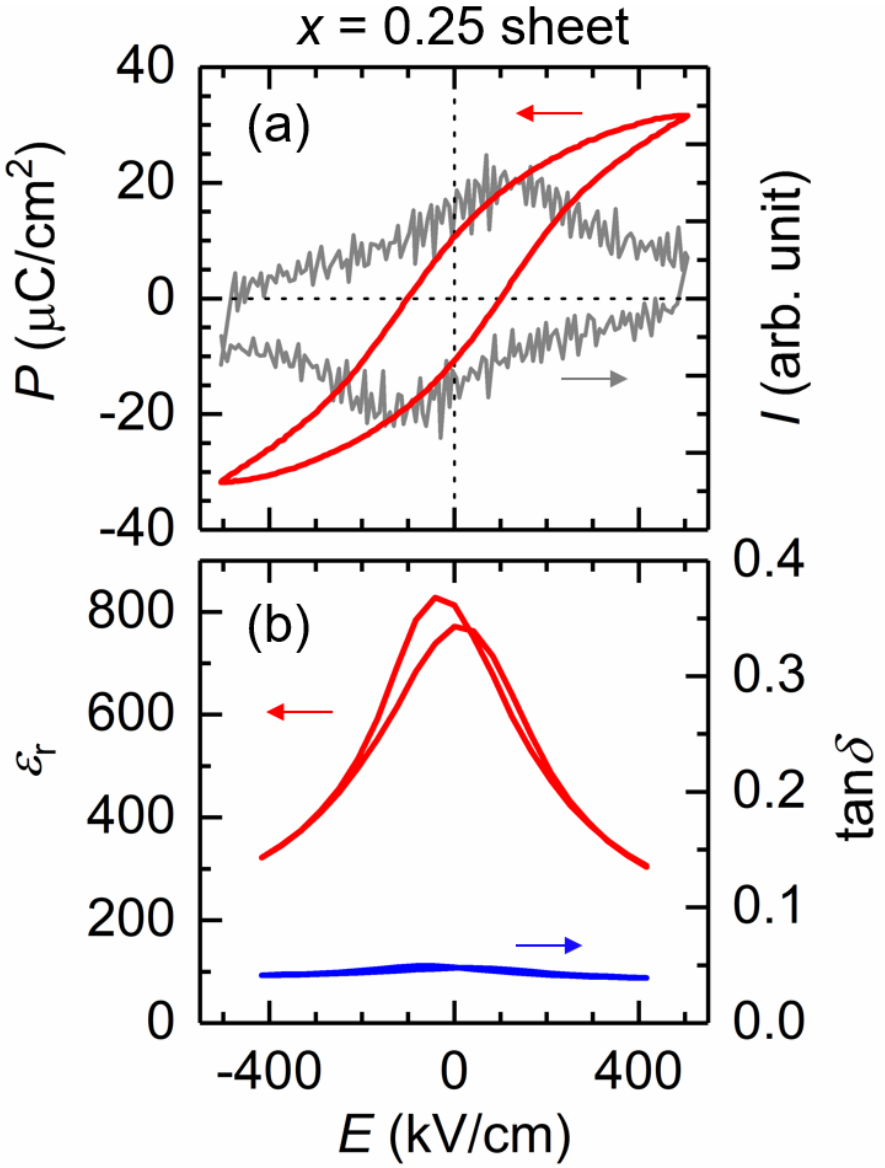

Figure 4-8. Ferroelectric and dielectric properties of BST x = 0.25 sheet. (a) P, I and (b) ε_r and tan δ values as a function of E for the $x = 0.25$ sheet at 25 °C. Poly-ITO electrode was used as the bottom electrode.

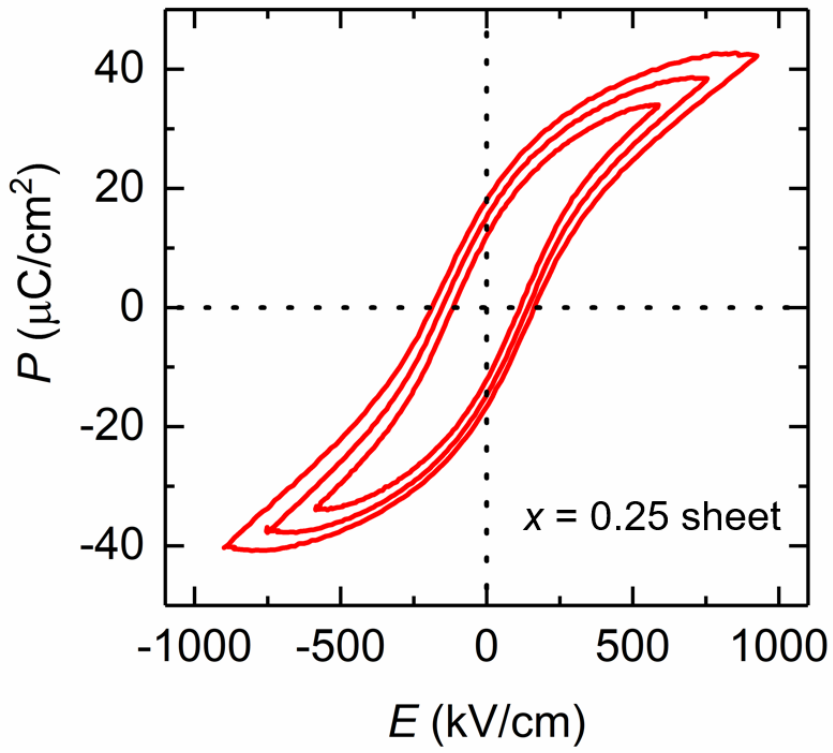

Figure 4-9. Ferroelectric property of BST x = 0.25 sheet with higher bias. The (a) *P*–*E* curves for the *x* = 0.25 sheet at 25 ºC. Polycrystal ITO electrode was used as bottom electrode.

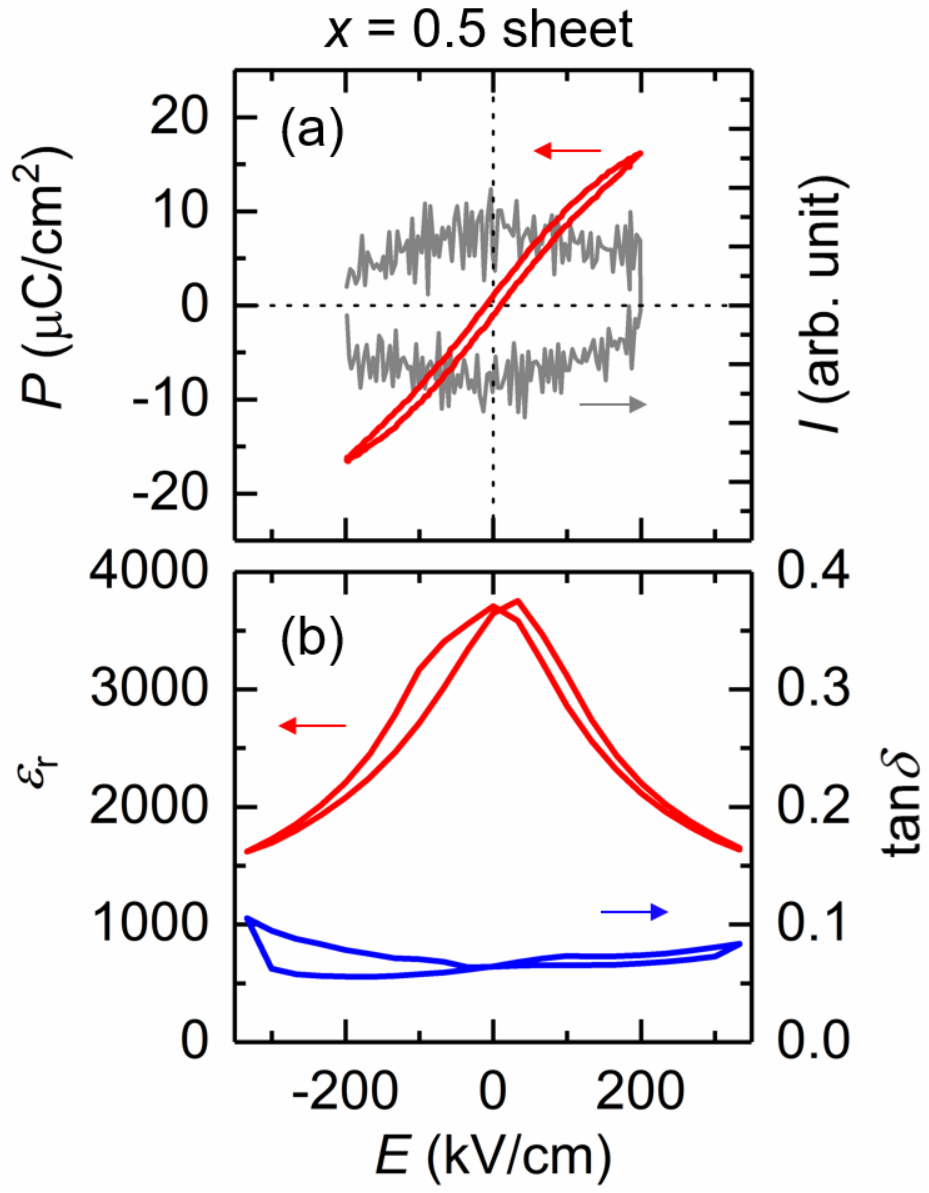

Figure 4-10. Paraelectric and dielectric property of BST x = 0.5 sheet. (a) P, I and (b) ε_r and tan δ values as a function of E for the x = 0.5 sheet at 25 °C. Poly-ITO electrode was used as the bottom electrode.

References

1. J. Jo, Y. Kim, T. Noh, J.-G. Yoon, T. Song, Coercive fields in ultrathin $BaTiO_3$ capacitors. *Appl. Phys. Lett.* **89**, 232909 (2006).

2. M. F. Ain *et al.*, 2.5 GHz $BaTiO_3$ dielectric resonator antenna. *Progress In Electromagnetics Research* **76**, 201–210 (2007).

3. M. Acosta *et al.*, $BaTiO_3$-based piezoelectrics: Fundamentals, current status, and perspectives. *Appl. Phys. Rev.* **4**, 041305 (2017).

4. H. A. Hamid, Z. Celik-Butler, Self-packaged, flexible, bendable MEMS sensors and energy harvesters. *IEEE Sens. J.* **21**, 12606–12617 (2021).

5. M. T. Todaro *et al.*, Biocompatible, flexible, and compliant energy harvesters based on piezoelectric thin films. *IEEE Transactions on Nanotechnology* **17**, 220–230 (2018).

6. M. P. Mahmud *et al.*, Advances in mems and microfluidics‐based energy harvesting technologies. *Adv. Mater. Technologies* **7**, 2101347 (2022).

7. N. Abbate, A. Basile, C. Brigante, A. Faulisi, in *2009 2nd Conference on Human System Interactions*. (IEEE, 2009), pp. 255–259.

8. S.-H. Yoon *et al.*, Grain-growth effect on dielectric nonlinearity of $BaTiO_3$-based multi-layer ceramic capacitors. *Appl. Phys. Lett.* **107**, 072906 (2015).

9. Y.-F. Zhu, L. Zhang, T. Natsuki, Y.-Q. Fu, Q.-Q. Ni, Facile synthesis of $BaTiO_3$ nanotubes and their microwave absorption properties. *ACS Appl. Mater. Interfaces* **4**, 2101–2106 (2012).

10. F. M. Chiabrera *et al.*, Freestanding perovskite oxide films: Synthesis, challenges, and properties. *Ann. Phys.* **534**, 2200084 (2022).

11. S. Kim *et al.*, Electrical properties and phase of $BaTiO_3$–$SrTiO_3$ solid solution. *Ceram. Int.* **39**, S487–S490 (2013).

12. J. Liou, B. Chiou, Dielectric characteristics of doped $Ba_{1-x}Sr_xTiO_3$ at the paraelectric state. *Mater. Chem. Phys.* **51**, 59–63 (1997).

13. X.-K. Wei *et al.*, Controlled charging of ferroelastic domain walls in oxide

ferroelectrics. *ACS Appl. Mater. Interfaces* **9**, 6539−6546 (2017).

14. S. Ruppi, A. Larsson, A. Flink, Nanoindentation hardness, texture and microstructure of α-Al_2O_3 and κ-Al_2O_3 coatings. *Thin Solid Films* **516**, 5959−5966 (2008).

15. G. A. Rosales-Sosa, A. Masuno, Y. Higo, H. Inoue, Crack-resistant Al_2O_3–SiO_2 glasses. *Sci. Rep.* **6**, 1−7 (2016).

16. D. Ugur, A. Storm, R. Verberk, J. Brouwer, W. Sloof, Kinetics of reduction of a RuO_2 (1 1 0) film on Ru (0 0 0 1) by atomic hydrogen. *Microelectron. Eng.* **110**, 60−65 (2013).

17. X.-Y. Zhang, P. Wang, S. Sheng, F. Xu, C. Ong, Ferroelectric $Ba_xSr_{1-x}TiO_3$ thin-film varactors with parallel plate and interdigital electrodes for microwave applications. *J. Appl. Phys.* **104**, 124110 (2008).

18. X. Zhou *et al.*, Microstructure and enhanced in-plane ferroelectricity of $Ba_{0.7}Sr_{0.3}TiO_3$ thin films grown on $MgAl_2O_4$ (001) single-crystal substrate. *Appl. Phys. Lett.* **89**, 232906 (2006).

19. H. Lu, L. Wills, B. Wessels, Electrical properties and poling of $BaTiO_3$ thin films. *Appl. Phys. Lett.* **64**, 2973−2975 (1994).

20. K. Bethe, F. Welz, Preparation and properties of (Ba, Sr) TiO_3 single crystals. *Mater. Res. Bull.* **6**, 209−217 (1971).

21. H. Alexandru, C. Berbecaru, A. Ioachim, L. Nedelcu, A. Dutu, BST solid solutions, temperature evolution of the ferroelectric transitions. *Appl. Surf. Sci.* **253**, 354−357 (2006).

22. Y. Zhang, G. Wang, T. Zeng, R. Liang, X. Dong, Electric field-dependent dielectric properties and high tunability of porous $Ba_{0.5}Sr_{0.5}TiO_3$ ceramics. *J. Am. Ceram. Soc.* **90**, 1327−1330 (2007).

23. R.-H. Liang, X.-L. Dong, Y. Chen, F. Cao, Y.-L. Wang, Effect of various dopants on the tunable and dielectric properties of $Ba_{0.6}Sr_{0.4}TiO_3$ ceramics. *Ceram. Int.* **31**, 1097−1101 (2005).

24. U.-C. Chung *et al.*, Low-losses, highly tunable $Ba_{0.6}Sr_{0.4}TiO_3$ / MgO composite.

Appl. Phys. Lett. **92**, 042902 (2008).

25. J. Cui, G. Dong, Z. Yang, J. Du, Low dielectric loss and enhanced tunable properties of Mn-doped BST/MgO composites. *J. Alloys Compd.* **490**, 353–357 (2010).

26. J. Qiu *et al.*, Structure and dielectric characteristics of continuous composition spread $Ba_{1-x}Sr_xTiO_3$ thin films by combinatorial pulsed laser deposition. *Ceram. Int.* **42**, 6408–6412 (2016).

27. H. Wu *et al.*, Effect of crystal orientation on the phase diagrams, dielectric and piezoelectric properties of epitaxial $BaTiO_3$ thin films. *AIP Advances* **6**, 015309 (2016).

Chapter 5. Summary

This doctoral thesis focused on transferring of high-quality flexible freestanding epitaxial sheet using amorphous oxide protection layer. Through this method, I have obtained the world's highest-quality single-crystal freestanding sheet.

In chapter 1, the background and purposes of this study are introduced.

In chapter 2, I report the significantly suppression of crack in LSSO sheet using an amorphous oxide protection layer. The results showed an a-Al_2O_3 is the most effective for crack suppression. Large-size crack-free LSSO sheets (up to 5 × 5 mm^2) was obtained using this lift-off and transfer method. The sheets could be transferred to various types of substrates, with a selection of the desired layer as the upper or lower side. The LSSO sheet exhibited a wide optical bandgap of 4.4 eV and a high σ value of 1600 S/cm at room temperature. Importantly, the expensive STO single-crystal substrates can be reused.

In chapter 3, I transferred millimeter-size crack-free LBSO sheet by employing the optimized a-Al_2O_3 protection layer despite of the large lattice mismatch. Furthermore, I controlled the shapes of the LBSO sheets such as rolled and flat forms. The rolled sheet had a tubular shape with diameter of 1 mm and length of 5 mm, while the size of the flat sheet was 5 × 5 mm^2. The presence of the a-Al_2O_3 protection layer allowed for a

significantly large crack-free area. The LBSO sheets exhibited wide optical bandgap of 3.5 eV and high Hall mobility of 80 $cm^2 V^{-1} s^{-1}$, making it promising for next-generation optoelectronic devices.

In chapter 4, I observed the enhancement of permittivity and tunability in freestanding BST sheets owing to release of substrate-induced strain, while keeping bulk-like ferroelectricity. Millimeter-sized BST epitaxial sheets were also obtained using an a-Al_2O_3 protective layer exceeding 10 nm in thickness. I found that poly- ITO is a suitable bottom electrode due to its high electrical conductivity and low deposition temperature. The $x = 0.25$ sheet demonstrated excellent ferroelectric properties, while the $x = 0.5$ sheet exhibited high permittivity and tunability, attributed to the absent of substrate-induced strain.

In short, I systematically studied on transfer of perovskite freestanding sheet. My research has accelerated the industrialization of single-crystal freestanding sheets and opened up new possibilities for exploring various intriguing properties of the perovskite freestanding single-crystal sheets.

Acknowledgements

This thesis was conducted under the supervision of Prof. Tsukasa Katayama at Research Institute for Electronic Science, Hokkaido University from April 2021 to March 2024.

First and foremost, I am deeply grateful to my tutor Prof. Katayama for the meticulous guidance and discussions during my doctoral studies. My tutor, a young and promising scholar, serves as a role model for my career aspirations. The harmonious and happy family life of my tutor also stands as an inspiration in my own life. I have a profound passion for my research career and am committed to dedicating my life to the pursuit of scientific research. However, in today's environment, achieving my ideals without outstanding research achievements seems challenging. I would like to express my gratitude once again to my outstanding tutor Prof. Katayama for guiding me with a sufficient quantity and quality of research papers, enabling me to continue my exploration in the academic. Encountering him has been a lifelong honor for me.

I would like to offer my special thanks to Prof. Hiromichi Ohta (RIES, Hokkaido niversity). In his laboratory, I acquired knowledge in various fields of condensed matter physics and learned how to operate many experimental instruments. I am deeply grateful to Prof. Ohta for providing me with abundant research equipment and guidance for my studies.

I would also like to express my sincere gratitude to Prof. Yamanouchi Prof. (formerly

at RIES, Hokkaido University, currently at IST, Hokkaido University), Hai Jun Cho (formerly at RIES, Hokkaido University until August 2022, currently at the University of Ottawa) and Prof. Yusaku Magari (RIES, Hokkaido University) for their invaluable guidance in scientific research and support in my daily life. Their extensive knowledge and research experience played a crucial role in steering my research endeavors in the right direction.

Next, I would like to thank all lab members I have worked together with in Ohta lab. Dr. Anup Kumar Sanchela (OB, Professor at Pandit Deendayal Energy U.) Dr. Yuqiao Zhang (OB, Professor at Jiangsu U.), Dr. Xi Zhang (OG, Professor at CQUT), Dr. Prashant Ghediya (Postdoc, RIES, Hokkaido U.), Dr. Takaki Onozato (OB, SONY), Dr. Gowoon Kim (OG, SAMSUNG ELECTRO-MECHANICS), Dr. Doudou Liang (OG, Professor at Ludong U.), Dr. Mian Wei (OG, Professor at Henan U.), Dr. Qian Yang (OG, Professor at Jiangsu U.), Dr. Binjie Chen (OG, specially appointed associate researcher at Wuzhen Lab.), (Mr. Yuzhang Wu (Ph.D candidate, IST, Hokkaido U.), Dr. Hui Yang (OG, Professor at Shenzhen Technology U.) , Mr. Zhiping Bian (Ph.D candidate, IST, Hokkaido U.), Mr. Kungwan Kang (Ph.D candidate, IST, Hokkaido U.), Mr. Koichi Sato (OB), Mr. Kenyu Sugo (OB), Mr. Yugo Takashima (OB), Mr. Takashi Fujimoto (OB), Mr. Liao Wu (OB), Mr. Rui Yu (OB), Mr. Yaoming Liu (Master candidate, IST, Hokkaido U.), Ms. Mitsuki Yoshimura (Master candidate, IST, Hokkaido U.), Mr. Ko Marunouchi (Master candidate, IST, Hokkaido U.), Mr. Ren Mitsuya (Undergraduate student, IST, Hokkaido U.), Ms. Ozaki (Secretary, Ohta lab) *et al.* for all the countless help during my

study and life. I would like to give special thinks to Dr. Yuqiao Zhang, Dr. Doudou Liang, Dr. Mian Wei, Dr. Binjie Chen and Dr. Hui Yang for instructing me in the operation of equipment in the Ohta lab and engaging in numerous beneficial scientific discussions.

I really appreciate the collaborations from Prof. Atsushi Taguchi (IST, Hokkaido U.) for measuring and conceiving the optical property of ferroelectric sheets.

I also appreciate the thesis committee members, Prof. Junichi Motohisa (IST, Hokkaido U.), Prof. Seiya Kasai (RCIQE, Hokkaido U.) and Prof. Toshihiro Shimada (Faculty of ENG., Hokkaido U.) for taking time to review this thesis and giving me valuable comments.

I do deepest appreciate to my friends met in Sapporo City, who accompany me through this memorable young period of my life as an international student. I hope for your future to be successful, happy, and fulfilling.

Finally, I appreciate the financial assistance from the China Scholarship Council (CSC), Japan, and the support extended by the Chinese Consulate General in Sapporo.

Lizhikun Gong

Sapporo, Japan

List of Publications

Publications related to this thesis

[1] **Lizhikun Gong**, Mian Wei, Rui Yu, Hiromichi Ohta, and Tsukasa Katayama*, "Significant Suppression of Cracks in Freestanding Perovskite Oxide Flexible Sheets Using a Capping Oxide Layer", *ACS Nano* **16**, 21013-21019 (2022).

[2] **Lizhikun Gong**, Rui Yu, Hiromichi Ohta, and Tsukasa Katayama*, "Synthesis and transparent conductivity of crack-free La:$BaSnO_3$ epitaxial flexible sheet", *Dalton Trans.* **52**, 6317 (2023)

[3] Rui Yu[#], **Lizhikun Gong**[#], Hiromichi Ohta, Tsukasa Katayama*, "Ferroelectricity, high permittivity, and tunability in millimeter-size crack-free $Ba_{1-x}Sr_xTiO_3$ flexible epitaxial sheets", *ACS Appl. Electron. Mater.* **5**, 5234–5239 (2023) (# Equally contributed to this work)

Other publications

[4] Mian Wei[#], **Lizhikun Gong**[#], Dou-dou Liang[#], Hai Jun Cho*, and Hiromichi Ohta*, "Fabrication and Operating Mechanism of Deep-UV Transparent Semiconducting $SrSnO_3$-based Thin Film Transistor", *Adv. Electron. Mater.* **6**, 2000100 (2020). (# Equally contributed to this work)

List of Presentations

[1] Lizhikun Gong, Bingjie Chen, Rui Yu, Hiromichi Ohta, Tsukasa Katayama, “ Flexible BaTiO3 Epitaxial Films with Bulk-like Ferroelectricity and Piezoelectricity”, “バルク様の強誘電性と圧電性を示す柔軟な $BaTiO_3$ エピタキシャル薄膜”, 第 84 回 応用物理学会 秋季学術講演会, 熊本城ホール+オンライン, 2023 年 9 月 19 日-23 日(招待講演).

[2] Lizhikun Gong, Bingjie Chen, Rui Yu, Hiromichi Ohta, Tsukasa Katayama, “ Flexible BaTiO3 Epitaxial Films with Bulk-like Ferroelectricity and Piezoelectricity”, “バルク様の強誘電性と圧電性を示す柔軟な $BaTiO_3$ エピタキシャル薄膜”, 第 70 回 応用物理学会 春季学術講演会, 上智大学 四谷キャンパス+オンライン, 2023 年 3 月 15 日-18 日(Oral).

[3] Lizhikun Gong, Mian Wei, Rui Yu, Hiromichi Ohta, Tsukasa Katayama, “Al_2O_3 保護層を用いた深紫外透明導電性 $SrSnO_3$ 自立シートの作製”, 2022 年 第 83 回 応用物理学会秋季学術講演会, 東北大学川内北キャンパス+オンライン, 2022 年 9 月 20 日-23 日(Oral).

[4] Lizhikun Gong, Mian Wei, Hiromichi Ohta, Tsukasa Katayama, “Transfer of oxide electrode sheet with wide bandgap of 4.6 eV “, 令和 3 年度日本セラミックス協会東北北海道支部研究発表会, online, 2021.11.18-19 (Oral).

[5] Lizhikun Gong, Mian Wei, Hiromichi Ohta, Tsukasa Katayama, “Transfer of oxide electrode sheet with wide bandgap of 4.6 eV”, 薄膜材料デバイス研究会 第 18

回研究集会 in 京都, オンライン, 2021.11.11-12(Oral).

List of Awards

[1] 第 70 回応用物理学会春季学術講演会 講演奨励賞 発表題目「バルク様の強誘電性と圧電性を示す柔軟な $BaTiO_3$ エピタキシャル薄膜」